Hybrid Magnetic Nanostructures (MNS) for Magnetic Resonance Imaging Applications

Mrinmoy De[a], **Stanley S. Chou**[a], **Hrushikesh M. Joshi**[a], and **Vinayak P. Dravid**[a]
Vinayak P. Dravid: v-dravid@northwestern.edu
[a]Department of Materials Science & Engineering, International Institute for Nanotechnology, Northwestern University, Evanston, IL 60208. Fax: +1 847 467 6573; Tel: +1 847 467 136

Abstract

The development of MRI contrast agents has experienced its version of the gilded age over the past decade, thanks largely to the rapid advances in nanotechnology. In addition to progress in single mode contrast agents, which ushered in unprecedented R_1 or R_2 sensitivities, there has also been a boon in the development of agents covering more than one mode of detection. These include T_1-PET, T_2-PET T_1-optical, T_2-optical, T_1–T_2 agents and many others. In this review, we describe four areas which we feel have experienced particular growth due to nanotechnology, specifically T_2 magnetic nanostructure development, T_1/T_2-optical dual mode agents, and most recently the T_1–T_2 hybrid imaging systems. In each of these systems, we describe applications including *in vitro*, *in vivo* usage and assay development. In all, while the benefits and drawbacks of most MRI contrast agents depend on the application at hand, the recent development in multimodal nanohybrids may curtail the shortcomings of single mode agents in diagnostic and clinical settings by synergistically incorporating functionality. It is hoped that as nanotechnology advances over the next decade, it will produce agents with increased diagnostics and assay relevant capabilities in streamlined packages that can meaningfully improve patient care and prognostics. In this review article, we focus on T_2 materials, its surface functionalization and coupling with optical and/or T_1 agents.

1. Introduction

Molecular-diagnostic imaging, a field at the intersection of biology and nanomedicine, has received considerable attention in the past decades for its diagnostic and clinical promises. More specifically, these techniques hold promise because they may elucidate relevant disease information and engender advanced diagnostic techniques for a wide spectrum of afflictions, and at a length scale ranging from sub-cellular to *in vivo*. Molecular imaging is one of the most popular (noninvasive) methods to allow real-time visualization of cellular functions of living organisms and related molecular interactions. For many imaging applications, especially *in vivo*, the development of imaging probes and contrast agents are particularly exciting. Realizing the importance of this technique, various probes and contrast agents have been developed for noninvasive imaging modalities; such as X-ray computed tomography (CT) [1], optical imaging, positron emission tomography (PET) [2], single-photon-emission computed tomography (SPECT) [3], ultrasound and magnetic resonance imaging [4], among others. Of these methods, MRI is currently one of the most powerful

diagnostic tools in medical science due to its ability to acquire 3-D tomographical information in whole tissue samples, including human soft tissues and whole animals, at high spatial (and temporal) resolution [5]. As MRI images are acquired without the use of ionizing radiation (x-ray/CT) or radiotracers (PET and SPECT), it has been the preferable imaging technique for heart, brain and nervous system. Important illustrative examples include assessment of irregular cardiac function, and detection of brain tumors [6, 7].

Despite the many advantages MRI currently enjoys, there remain many challenges for more efficacious diagnostic imaging of localized diseases. For example, although tissue MRI is capable of revealing anatomic details in organs, often it is difficult to differentiate the normal and diseased cells due to small native relaxation time differences. In this context, imaging sensitivity can be enhanced with the use of MRI contrast agents. Traditionally, there are two classes of MR contrast agents available, T_1 and T_2. T_1 contrast agents increase the T_1 relaxation time, resulting in hypersignal, giving bright contrast T_1-weighted images. On the other hand, T_2 contrast agents reduce T_2 relaxation times, which reduces both T_2 and T_2^* signals, giving rise to dark contrast T_2-weighted images. T_1 contrast agents are paramagnetic in nature, such as gadolinium (Gd^{3+}) and manganese (Mn^{2+}) chelates. Among them, Gd^{3+} complexes are more widely used for clinical application such as brain tumor contrast enhancement requiring the breakage of the blood-brain barrier. For instance, gadolinium-diethylene-triamine penta-acetic acid (Gd-DTPA) is one of the most commonly used T_1 contrast agents in clinical MRI imaging due to its physiological inertness and non-selective extracellular distribution [8]. It is routinely used in a wide variety of MRI applications, including selective enhancement of specific tissues, fluid compartments and lesions. Superparamagnetic materials, such as magnetite (Fe_3O_4) nanoparticles act as a T_2 contrast agent.

Recent advances in cross-disciplinary nanoscience and nanotechnology have led to further and rapid developments of new "nanohybrids" as probes for molecular imaging [9]. Here, we define "*nanohybrids*" as nanometer scale composite structures that combine "*hard*" magnetic oxide nanostructure with one or more "*soft*" (molecular/polymeric/biological) structures for enhanced efficacy for effective cellular/molecular targeting and potentially additional attributes, such as thermal activation, drug release, among others.

The advancements in probes, with progressing imaging capabilities, have subsequently engendered tremendous progress in imaging technology. MRI probes based upon nanomaterials are unique in certain regards, because they take advantage of property changes that occur when materials are scaled below ~100 nm, principally they include high surface to volume ratio, controllable crystal growth and quantum confinements. The high surface area enhances physical interactions, chemical loadings and reactivity. Nanosized shapes and sizes derived from controlled crystal growth directions allow different extent of molecular recognition, bio-distribution and bio-degradation. Quantum-confinement of the material generates unique size-dependent electronic, magnetic, and optical properties depending on their chemical composition, shape and size. Magnetic nanostructures (MNS), such as magnetite nanoparticles, represent the first nanoparticulate T_2 agents. Separate from single function MRI probes, hybrid multimodal imaging agent are also being developed using a combination of optical and magnetic properties or a combination of T_1 and T_2; and related combinative modalities [10, 11].

Compared to conventional MRI imaging agents, nanostructure-based agents offer a number of advantages. First, through surface modifications, bio-stability and tunable bio-distribution can be achieved. Second, through shape, size and composition tuning, different degrees of biocompatibility and imaging properties can be tailored. Third, nanostructures can be targeted for specific biomarkers through complexation with antibodies and other targeting

agents. Fourth, conjugation with probes with alternate imaging properties can allow multimodal imaging. In citing these advantages, however, it is important to remember in the absence of extensive surface modifications, MNSs are inherent contrast enhancers due to their intrinsic native properties, and there are many examples in literature where they were used without extensive modifications. In this review, we highlight the current progress in preparation and application of MNS as nanohybrid MRI contrast agents. We classified those nanohybrids as (i) T_2 MRI hybrids, [12] T_1 MRI nanohybrids and (iii) Dual modality MRI nanohybrids (Figure 1).

2. T_1 MRI nanohybrids

Although T_1 and T_2 weighted imaging are somewhat self-complementary, T_1 contrast agents have some advantages over T_2 agents. For example, the T_2 hypo-intensity (dark contrast) can be confused with other physical irregularities such as cavities, blood accumulation and metallic deposits. Similarly, owing to the fact that many T_2 agents possess significantly higher relaxivities than T_1 agents, the resultant signal perturbations may lead to imaging artifacts present in adjacent tissues (although artifacts may be present in either T_1 or T_2 systems). On the other hand, T_1 contrasting agents also have limits. For example, limited accessibility of Gd(III) complexes in the blood pool and extracellular space is major disadvantage of the Gd(III) based contrast agents. Some of these disadvantages can be overcome by conjugating T_1 contrast agents to nanostructures. This route can concentrate Gd(III) ion on the nanostructures and enhance the T_1 signal, it can also increase the cellular uptake of Gd(III) ions through size and shape tuning of the vehicle nanostructure. Further, by conjugating with bio-activable linkers, dynamic biomolecular phenomena can be imaged utilizing chemically-induced activation of T_1/T_2 agents in the presence of biochemical reaction and signaling.

Recently various efforts have been reported in which Gd(III) complexes were attached to nanostructures based on silica [13], TiO_2 [14], gold [15], dendrimer [16], nanodiamond [17], polymer [18] etc. For example, although TiO_2 is best known for its photo-catalytic and chemical properties, Endres *et. al.* have shown that TiO_2-Gd(III) complexes are biocompatible and therapeutically active carriers that can be detected by MRI [19]. In this work, surface of the TiO_2 labeled with DNA nanostructures were modified by Gd(III)-DOTA (1,4,7-tris(carboxymethylaza)cyclododecane-10-azaacetylamide) via ortho-substituted enediol ligands. Relaxivity of resulting conjugate was 3.5 0.1 mM^{-1}s^{-1} per Gd(III) ion (1.5 T) equivalent to the DOTA molecules used to functionalize the TiO_2. From detailed characterization, an R_1 relaxivity of 61.0± 1.7 mM^{-1}s^{-1} per nanostructure was observed. Cellular studies using PC12 cells and x-ray fluorescence spectroscopy revealed that these conjugates tend to remain in the cytoplasm (and not the nuclear region) after transfection. Elemental fluorescence signals and toxicity assays indicated that these conjugates are biologically compatible. In the cellular MR imaging studies, cells incubated with these conjugates show better T_1 contrast in T_1 weighted images over control cells, thus demonstrating effective contrast enhancement. In another example, Manus *et. al.* recently coupled amine functionalized Gd(III) complex with nanodiamonds through carboxylic group present on the nanodiamond surface [17]. This conjugate demonstrated a significantly reduced T_1, resulting in a R_1 relaxivity of 58.82±1.18 mM^{-1}s^{-1} per Gd(III) complex. Interestingly, it showed a tenfold increase in relaxivity as compared to monomer Gd(III) complex; among the highest relaxivity ever reported for the Gd(III) complexes. These highlights are among several notable recent reports on T_1 advancements in MR imaging. As this article focuses on T_2 and multimodal imaging agent (T_1-optical, T_2-optical), we refer interested readers to other review articles for T_1 specific nanohybrids [10, 11, 20, 21].

3. T_2 MRI nanohybrids

Unlike T_1 agents, which retard longitudinal proton relaxation, T_2 agents expedite transverse relaxation through loss of coherence. In T_2 weighted images, T_2 contrast agents attenuate signal intensity, and therefore appear dark. The rate (R_2) at which T_2 agents attenuate the signal can be described according to equation 1 below, where T_2 is defined as the observed transverse relaxation time. Additionally, T_2^o is the T_2 in absence of contrast agents; C is the agent concentration and χ is the relaxivity of the material. The relaxivity of the T_2 agents can therefore be determined by taking the derivative or R_2 with respect to concentration [22].

$$R_2 = \frac{1}{T_2} = \frac{1}{T_{2o}} + \chi C$$

Because flocculation and agglomeration of individual nanocrystals may occur *in vivo* or *in vitro*, the term T_2^* is also often utilized to differentiate from pure molecular effects (T_2). If aggregation is done in a controlled fashion, a flocculated bunch including several individual magnetic crystals may be considered as single magnetic nanostructure (MNS). A generalized equation to account for the magnetic coupling effect found in agglomerates is described below [23], where μ_{sp} is the magnetic moment of one nanocrystal and N_g is the number of nanocrystals per agglomerated structure. μ_o is the permittivity of free space. γ is the proton gyromagnetic ratio. N_A is Avogadro's number. C_a is the agglomerate concentration. R_a is the agglomerate radius. D the diffusivity of water, and L(x) the Langevin function with respect to $X = \mu_{sp}N_gB_o/(kT)$. It can be seen then, that R_2 is proportional to the *square* of individual magnetic moments (μ_{sp}) and the number of particles in each aggregate N_g.

$$R_2 = \frac{1}{T_2} = (\mu_{sp}N_g)^2 \left[\frac{64\pi}{135} \right] \left[\frac{\mu_o \gamma L(x)}{4\pi} \right]^2 \left[\frac{N_A C_a}{R_a D} \right]$$

The effect of enhanced T_2 due to agglomeration has been exploited by Perez and Weisledder for MRI sensors [24, 25]. In these cases, nanostructures are designed to aggregate with target analytes. These aggregations are detectable through changes T_2 relaxation time (MRI contrast). Similarly, controlled aggregation during synthesis can be exploited to engineer the transverse relaxivity of each nanostructure. In a recent report, Meade's and Bahadur's group reported synthesis of magnetite (Fe_3O_4) "nanoflowers", with each nanoflower formed through the controlled aggregation of individual nanocrystals during synthesis [26, 27]. The R_2 values of these nanostructures measured at 1.5T are 148 $mM^{-1}s^{-1}$ (42 nm), 238 $mM^{-1}s^{-1}$ (30 nm) and 126 $mM^{-1}s^{-1}$ (19 nm). In this case, the deviation from ideal agglomeration properties can be attributed to differences in primary Fe_3O_4 crystal size with the assemblies (4.3, 4.8 and 4.5 nm for 42, 30 and 19 nm nanoflowers), and consequently their differing μ_{sp} values (33, 45 and 36 emu/g Fe, respectively).

3.1. Magnetic nanostructure (MNS) – Role of size, shape and composition

In addition to the aggregation properties, the size and shape of the MNS cores also have precipitous effects on MRI performance. In studying how MNS sizes affect T_2 relaxation time, Jun *et al.* prepared 4, 6, 9 and 12nm Fe_3O_4 (magnetite) structures and observed saturation magnetization moments (μ_{sp}) of 25, 43, 80 and 101 emu/g Fe respectively [28]. The increasing μ_{sp} with size leads to shorter T_2 times (and therefore faster R_2). The trend

was attributed to spin canting on the surface of the MNS, that is, as surface to volume ratios decrease with increasing particle size, disordered spins on MNS surfaces play a smaller role, resulting in increased μ_{sp}. This same trend was observed by Morales *et al.*, on polydispersed γ-Fe_2O_3 structures [29].

Using $CoFe_2O_4$ (cobalt ferrite) MNS as a *model* system, we have investigated the effect of size and shape on magnetic performance[30]. By synthesizing cobalt ferrite MNS in the presence of a magnetic field during thermal decomposition, we were able to create faceted irregular (FI) MNS in additional to traditional spherical MNS. In this manner, spherical Cobalt ferrites with 6, 10 and 15 nm diameters and FI Cobalt ferrites 12, 25 nm were prepared (Figure 2A). In comparing R_2 versus μ_{sp}, it was observed that with a given μ_{sp}, FI structures appear to exhibit greater R_2 relaxation rates. Furthermore, it was observed that given similar size, FI structures have lower μ_{sp} values (Figure 2B, C). We attribute these effects to the differences in surface-to-volume ratios between spherical MNS and FI MNS, with FI generally higher than spheres. This resulted in an increased surface spin canting effect, thereby reducing the overall magnetization. Similarly, while the overall magnetization is reduced, the increased surface area also allows a greater number of hydrogen nuclei of water in proximity. Therefore, a greater number of neighboring nuclei were disturbed by the nanostructure magnetic field, resulting in faster relaxation.

In regards to the compositional impact of metal dopants in ferrite structures, Lee and Cheon, et. al., prepared 12 nm $MnFe_2O_4$, Fe_3O_4 (magnetite), $CoFe_2O_4$, $NiFe_2O_4$. In all, it was found that $MnFe_2O_4$ demonstrated enhanced magnetization values over the more commonly used magnetite (110 emu/g Fe vs. 101 emu/g Fe). Following that trend, an increased R_2 value was also observed (218 vs. 172 $mM^{-1}s^{-1}$). In contrast to Mn doping, Co and Ni doping resulted in reduced magnetization and R_2 values [31].

3.2. Stabilization and Surface Functionalization

Perhaps the most challenging aspect of applying magnetic nanostructures *in vitro* and subsequently *in vivo* involves surface functionalization for efficacious molecular and cellular targeting. In addition to colloidal stability and shelf-life, surface functionalization also plays a prominent role in defining a nanostructure's behavior in the target system, including cellular internalization, targeting, epsonization, and bio-compatibility. Designing a properly functionalized structure is therefore of paramount importance. Generally speaking, surface functionalization of MNS can be classified in regards to inorganic (silica), carbohydrate (Dextran), or single monomer/polymer grafted onto MNS surfaces through chemically specific bindings. Each functionalization method has its benefits and drawbacks and requires trade-offs and optimizations. For example, although silica coatings can provide colloidal stability, it may also retard R_2 relaxation [32].

3.2.1. Silica coating and functionalization—Silica coating of iron oxide MNS is popular as evidenced in the literature because of their ease of synthesis and resultant aqueous stability. Most typically, the hydrolysis and subsequent condensation of tetraethoxysilane (TEOS) based precursors were used [32–36]. This process is alternatively known as the Stober process. Thickness of the silica shell can be controlled by varying the ratio of ammonium hydroxide, TEOS and reaction time, achieving nanometer length precision. The resultant structures have a strong negative charge across a wide range of pH, and are stabilized in water through coulomb repulsion [32, 37]. Adopting strategies for functionalizing silica, alkylsilane molecules can be used to modify silica-MNS surfaces, and impart additional functionality, thereby enabling targeting and labeling possibilities. A popular modification is the addition of 3-aminopropyl-triethoxysilane (APS) to the TEOS precursors, which creates silica shells with primary amine groups [38, 39].

Using this method, we were able to achieve good thickness control over silica coatings on cobalt MNS cores (Figure 3). Subsequent functionalization of silica coated MNS though silane chemistry is also possible. Similarly, by reacting APS with isothiocyanate functionalized fluorescent dyes (which reacts with the primary amine on APS) prior to mixing with the Stober precursor (TEOS), Lu *et al.* [33] were able to incorporate additional functionality (fluorescence, in this case) to their silica-MNS nanostructure, further diversifying potential methods in modifying silica coated MNS. Currently, MNS with inert silica coating is available as ferumoxil (AMI-121), an orally ingested T_2 contrast agent for delineation of the intestinal loops from adjacent tissues and organs, as pancreas and anterior kidney [40–43]. Ferumoxil is also known by the trade names GastroMark and Lumirem.

As briefly mentioned previously, one aspect of silica coating on MNS that may not be immediately obvious relates to the prolonging of T_2 relaxation time with thicker silica shells due to reduced interaction with water molecules. Because this effect is likely to be observed in many other surface functionalization schemes, it is particularly worth highlighting. As silica coating through the Stober method allows nanometer control [33, 44], effects of coating thickness on MR can be explored systematically. Using this method, Pinho *et al.* recently observed a tenfold decrease in r_2, from 228 mM^{-1}s^{-1} to 23 mM^{-1}s^{-1}, in the first 20nm of silica coating a 10 nm γFe_2O_3 core (Table 1) [32]. Here, Pinho *et al.* attribute the decrease in relaxivity to outer sphere relaxation effects. Specifically, Pinho *et al.* deduced that there are two regions of silica shell coating, an inner water-impermeable layer of up to 40 nm, and an outer water-permeable layer. Because of the impermeable layer, proton interaction with the magnetic core was reduced significantly [32] (Table 1). In short, the silica shell places a barrier between the magnetic core and protons, thereby reducing relaxivity. We speculate that this effect pertains not only to silica coating, but may be observed in the systematic study of other systems. It is therefore likely that this optimization between stability and relaxivity will require certain balance in design.

3.2.2. Carbohydrate coating (Dextran)—Dextran is a branched polysaccharide consisting of multiple glucose units linked through α-1,6 glycosidic linkages. It was first used as a MNS coating by Molday and McKensie in 1982 through in-situ coating of iron-oxide during the co-precipitation process [51]. The resultant structures, consisting of 15 nm cores and 30–40 nm overall size, were found to be stable against aggregation in physiological buffer, and were used as a label for magnetic separation of cells. Subsequent iterations of the Molday method produced ferumoxtran-10 (AMI-277) and ferumoxides (AMI-25). These two structures both have cores of ~5nm, but differ significantly in dextran coating thickness (20–40 nm versus 80–150 nm) [52]. The differences in dextran thickness provide changes in physiological retention. Ferumoxtran, with the smaller diameter, showed prolonged retention in humans, with half-life in excess of 24 hrs [52]. This stands in contrast with ferumoxides, whose half-life is ~2hrs [53]. The overall structure size also appears to effect cellular uptake. In comparing monocyte uptake of ferumoxtran-10 and ferumoxides, Metz, *et al.* [54], incubated human monocytes with MNS at concentrations of 100 μg/ml and reported uptake of ferumoxtran-10 to be ~2 pg Fe/cell, and ferumoxides to be 8.9 pg Fe/cell, demonstrating preferential phagocytosis of larger structures. In both cases, the dextran molecules are adhered non-specifically to the iron oxide surface through hydroxyl interactions with the iron oxide core. Hydrogen bonds along the length of the dextran molecules provide strengthened interaction to prevent the desorption of the dextran coating. Despite the hydrogen bonds, however, desorption effects can still be observed in high dilutions [55]. To combat this effect, the dextran molecules can be chemically cross-linked [56]. Cross-linked and non-cross-linked dextran-MNS show virtually identical properties [56]. In addition to post absorption cross-linking, dextran chains can also be modified to include carboxyl groups and take advantage of their higher affinity towards iron oxide

surfaces. Using this strategy, ferumoxytol [47] and ferucarbotran [45, 57] have been commercialized.

3.2.3. Nonspecifically absorbed and chemically anchored mono/polymers—As stated previously, because increasing coating thicknesses can negatively impact R_2 and expedite phagocytosis and particle clearance, there is a need to develop alternative surface functionalization methods. To tackle this problem, Poly ethylene glycol (PEG) based ligands are often the first choice given their biocompatibility, and because it is well known that PEG ligands can stabilize metallic particles under physiological conditions [4, 58–61]. PEG grafting may be achieved by single-point chemical anchoring through functional groups such as carboxylates, phophonates, dopamine or dopa, or they can be nonspecifically absorbed on to MNS surfaces.

Chemical anchoring approaches take advantage of chemical affinities towards iron oxide surfaces to impart monolayer functionality. Commonly, this has been demonstrated through silanes, carboxylates, phosphate derivatives and dopamine. Most recently, nitro-dopamine has been also proposed as an ultra stable chemical anchor. With regard to silane anchored ligands, Kohler *et al.* stabilized magnetite MNS though the usage of trifluoroethylester-terminated PEG silane [62]. In that work, hydrophobic ligands were exchanged with the hydrophilic ones (trifluoroethylester-terminated PEG silane), owing to the silane-magnetite affinity, providing colloidal stability in the aqueous phase.

The ligand exchange approach is typical of chemically anchored ligand functionalization, as it allows separate optimization of ligand and MNS core synthesis conditions. PEG with phosphine-oxide anchors have been used by Kim *et al.* to functionalize maghemite (γ-Fe_2O_3) and impart aqueous stability [63]. Similarly, dopamine can also be used as a chemical anchor for iron-oxide surfaces [64]. In particular, as related to PEG'lated functionalization, Peng and Sun reported bifunctional PEG with dopamine and carboxylate termini undergoing successful ligand exchange with hydrophobic Fe-core: Fe_3O_4-shell MNS synthesized in the organic phase [65]. In this experiment, it is expected that dopamine will outcompete carboxylates in Fe_3O_4 attachment, due to their higher affinity. With an outer carboxylate group exposed, the particles should be negatively charged in physiological pH, imparting colloidal stability through coulomb repulsion. Similarly, Xie and Sun also reported monomethoxy-poly(ethylene glycol) 2000 conjugation to dopamine through trichloro-*s*-triazine, producing a ligand capable imparting aqueous colloidal stability to Fe_3O_4 MNS [66]. Stability in PBS buffer was reported in both cases.

Amstad *et al.* recently reported a systematic study on the influence of anchor groups on PEG(5), 5kD, stabilized magnetite MNS [67]. In all, stability of nine different anchor groups was included in the study. Most notably, they include carboxylates, dopamine, and nitrodopamine, three of the most popular anchors in literature. Using successive filtrations using a 200nm cut-off filter as a measure of binding reversibility of the anchor groups, it was found that PEG(5)-COOH functionalized MNS cannot pass through the filter. Furthermore, dopamine functionalized particles, can only survive zero to three filtration cycles. This stands in contrast with nitro-dopamine, which survived in excess of nine filtration cycles. The higher affinity of nitro-dopamine binding also manifests itself in Thermal gravimetric analysis (TGA) and XPS, where generally good agreements with filtration results were observed. A summary of the ligand packing density and filtration stability from this study can be found in figure 4.

Lastly, concerning the nonspecifically absorbed PEGs, it is most notably used in the polyol synthesis, in which PEG polyols, such as triehtylene glycol (TREG), are used in a triple role as a high-boiling point solvent, reducing agent, and surface passivator to control particle size

iron oxide precursors, such as iron (III) acetylacetonate. In the case of MNS produced through the TREG-polyol method, Wan *et al.* reported water soluble Fe_3O_4 (magnetite) cores in the range of 7–8 nm. These MNS are reported to be stable in PBS buffer [49, 68].

3.3. Applications of MNS probes in MR imaging

Tracking of cell fates *in vivo* has long been of medical interest. By loading cells with MNS prior to implantation, it is now demonstrated that this is a feasible concept through MR imaging. Initial reports in this area centered around non-specific endocytosis of dextran coated MNS *in vitro* prior to imaging [69] or introduction in to *in vivo* models [70, 71]. In the past six years, cell fate monitoring with MNS has been used in transplanted rat bone marrow stromal cells (rMSC) and human embryonic stem cell in rats (*in vivo*) [72, 73], human mesenchymal stem cells (hMSCs) and CD34+ hematopoietic stem cells (HSC) in mice (ex vivo) [74], tracking neural stem cells in patients [75]. Tracking single cells *in vivo* has also been demonstrated [76, 77]. In the initial report by Jendelova *et al.*, regarding MSC transplantation in rats [72, 73], Endorem®, a trade name for ferumoxide, with no additional modification were incubated with rat rMSC cells *in vitro* for 72 hours prior to transplantation [72]. The uptake by the cells was non-specific and determined to be ~17.5 pg Fe/cell, corresponding to 20–30 MNSs. Labeled cells were then grafted intracerebrally onto the contralateral hemisphere of adult rat brains. The resulting hypointense signal was observed *in vivo* in excess of 50 days using a 4.7 T Bruker spectrometer. Later, this work was extended by Jendelova *et al.* to include MSC and ESC cells grafted and administered intravenously to rat models [73].

Arbab *et al.* has also reported ferumoxide labeling of human mesenchymal stem cells (hMSC) and CD34+ hematopietic stem cells (HSC) [74]. In this report, the transfection of ferumoxide was enhanced by electrostatic incorporation of cationic protamine sulphate (PS), the result of overall zetapotential change from anionic to cationic with increasing PS loadings. It is well known that cationic nanoparticles have enhanced uptake. Ferumoxides-PS complexes were formed by mixing prior to addition to cells. Following overnight incubation with at 50:3 Ferumoxide: PS MNS complex, HSC uptake of MNS was shown to be from 2.01 ± 0.10 pg Fe/cell. Similarly, hMSC showed uptake of 10.94 ± 2.86 pg. Little to no loss in proliferative capacity of cells was observed following incubation as measured through MTT assay. Tracking of HSC cells ex vivo, 14–15 days after initial tumor xenograft and tail vein injection of MNS labeled HSC cells showed hyposensitivities, demonstrating MNS retention.

Neural stem cells tracking in human patients using ferumoxide has also been reported [75]. In this case, neural stem cells were incubated with ferumoxide and Effectene®, a lipofection reagent, for 60 minutes prior to implantation into patients, into areas with brain damage. After implantation, hypointensities were observed, with decreasing intensity over time, until the 7th week. The decrease in signal was attributed to dilution effects due to cell proliferation. To detect single cells *in vivo*, Heyn *et al* [76]. used ferumoxide and JT774 macrophage cells to achieve elevated loadings. After 24 hour incubation, cells with loading of 60.9 ± 1.6 pg Fe/cell were injected in to the left ventricle of mice. Using a 1.5T GE/I whole-body clinical MRI scanner, mouse brains were imaged 5hrs after injection. To confirm single cell detection, mouse brains were examined again *ex vivo* via MRI. Confocal microscopy was used to confirm signal intensities resulted from individual cells.

Beyond nonspecific endocytosis, it is also possible to use MNS in targeted imaging. In an earlier report, Artemov *et al.*, used MACS streptavidin microbeads (50 nm polysaccharide coated iron oxide MNS, 50–59% iron oxide w/w pre-functionalized with strepavidin) conjugated with biotinylated Her-2/neu antibody Herceptin to target tyrosine kinase her-2/neu receptors in a panel of breast cancer cells *in vitro* [78]. Contrast observed in MR image

was found to be proportional to the expression level of kinase her-2/neu receptors for the given cell lines. In this case, because the MNS have cell surface targeting moieties, the MNS were found at the surface of the cells, rather than internalized. More recently, McAteer *et al.* used antibody conjugated MNS to detect vascular cell adhesion molecule-1 (VCAM-1), mediators of mononuclear leukocyte recruitment and lesion initiation in multiple sclerosis, in live mouse models [79]. In these experiments, MNS was administered by tail vein injection, after VCAM-1 expression was induced in one brain hemisphere. Remarkably, stark contrast in hypointensities became apparent on the activiated hemisphere, with little non-specific retention in the non-activated half. Controls confirming *in vivo* targeting were performed using non VCAM-1 targeting MNS (IgG conjugated MNS), and separately, injecting unbound VCAM-1 antibodies to saturate VCAM1 prior to injecting VAN1 antibody functionalized MNS.

It is also possible to use MNS for detection of analytes, via MRI imaging. As mentioned briefly, Perez and Weisledder demonstrated this by taking advantage of changes in R_2 due to MNS aggregation [24]. In sensing oligonucleotide interactions, MNS were first conjugated with DNA, and introduction of complementary sequences induce aggregation, and is therefore detectable as MRI contrast. Furthermore, antibody functionalized MNS can be induced to aggregate with target analytes. In this case, MNS functionalized with multiple (~8) anti-GFP polyclonal antibodies was incubated with GFP protein and used to show changes in R_2. Incubation with BSA using the same antibody showed no change is R_2. Sensing enzymatic activity was demonstrated by first aggregating MNS using an ezyme targeted peptide/protein. Introduction of the enzyme then cleaves the aggregation, releasing individual MNS, resulting in whiter contrast. In the DNA induced aggregation experiments, 0.5 fmol of oligo in 50 μl volume induced detectable signal change. More recently, Yigit *et al.* applied a similar detection theme towards human thrombin [80]. By attaching DNA-aptamer recognizing the fibrinogen-recognition exosite of thrombin to one set of MNS, and aptamer recognizing the heparin-binding exosite of thrombin to a separate set of MNS and mixing them in a 1:1 ratio, a solution of MNS which will aggregate upon addition of thrombin was created. Using this method, Yigit *et al.* was able to detect 25 nM of thrombin using a 4.7 T NMR machine.

4. Dual-modality MRI nanohybrids

Although MRI is a great imaging technique for visualizing biological tissue and activity, it is not always sufficient in providing all the necessary information. As no single imaging modality can provide all requisite information in every application setting, multimodal molecular imaging agents have been gaining significant traction [10, 11]. Herein, multimodal imaging agents are defined as probed that enable a synergistic combination of two or more detection techniques in image collection or enhanced data acquisition relevant to diagnostics. Most typically, dual modal MRI agents combine magnetic imaging with fluorescence, PET or SPECT. For example, fluorescence can be of assistance in surgical settings, while PET or SPECT imaging can assist MRI in identifying and tracking tumor cells and physiological processes. In this regard, nanoparticulate vehicles can be used to combine different imaging probes in a single confinement. In this report we consider two kinds of dual modality approaches which includes (i) nanohybrids combining fluorescence and T_1/T_2 MRI agent [12] and (ii) nanohybrids that combine T_1 and T_2 capabilities. Separately, not covered in detail this review, are also dual modal agents that combine PET and MRI [81]. PET and MRI are largely complementary techniques and process the data in similar fashion. The PET-MRI system is desirable because while PET is very concentration sensitive, it has poor resolution as compared to MRI, which can provide high resolution anatomic information in sub-millimeter range. There are drawbacks however, as PET-MRI systems can observe from the unwanted interference between the PET radiofrequencies and

MRI magnetic fields. Despite these interferences, there is reported success based on MR-compatible PET system or multislice PET scanners [82].

Perhaps more popular than PET-MR are nanohybrids with MRI with optical imaging capabilities, such as fluorescence. Reports related to MRI-optical dual-modal agents are particularly abundant because as they combine the sensitivity of fluorescence assays with the spatial resolution of MRI. In current biological imaging prospective, fluorescence-MRI imaging is the most developed and well characterized dual modality imaging technique. The MRI-optical probe based imaging agents are typically a combination of paramagnetic chelates or magnetic nanostructures with fluorescence probes and/or quantum dots. Based on distinct MRI characteristics, we can separate optical-MRI nanohybrids in to T_1 and T_2 based optical imaging agents.

4.1. Optical-T_1 MRI agent nanohybrids

T_1 MRI agents are typically complexes of Gd^{3+} or Mn^{2+} ions stabilized by chelates, such as DTPA (diethylenetriaminepentaacetic acid) and DOTA (1,4,7,10-tetraazacyclododecane-N,N$'$,N$''$,N$'''$-tetraacetic acid) etc. [8, 83] In the initial reports regarding T_1 multimodal imaging agents, the chelating ligands were chemically modified to attach fluorescent probes such as FITC and rhodamine [84, 85]. In addition to common fluorophores, luminescent metal ions were also used. In one example, Koullourou *et al.*, reported a Heterobimetallic Rhenium-Gadolinium Complex, $[GdRe(Bpy)(CO)_3]^+$ [86]. In this complex rhenium was used as the luminescent chromophore and Gd^{3+} ion as the MRI probe. They observed that the luminescence lifetimes of rhenium ion are long enough (0.24 ms)to permit efficient gating of any fluorescent background (typical lifetimes are <10 ns) while the gadolinium ion were used to provide MR contrast. In another application Lippard's group used Mn^{3+} for multimodal sensing of Zn^{2+} ion [87]. Here, water soluble porphyrins chelate Mn^{3+} ions and Zn^{2+} ions to create a MR-fluorescence probe. Specifically, DPA (dipicolylamine, Zn^{2+}) and TPPS (5-phenyl-10,15,20-tris(4-sulfonatophenyl)porphine, Mn^{3+} receptor) were used. Here, the DPA acts as an excellent fluorescent sensor for zinc by increasing fluorescence intensity by more than tenfold. Additionally the manganese derivative of TPPS (TPPS$_3$Mn(III)) generate MRI signals. They also observed in the presence of zinc, the relaxivity of Mn complex in aqueous solution was significantly altered, making it a promising zinc MRI sensor. Both metal-free and Mn(III)-inserted forms are efficiently internalized by live HEK-293 cells and imaged by both fluorescence or MR.

Despite the successes of these reports, there are common problems associated with small molecule-based multimodal imaging agents. Firstly, these small molecule agents frequently suffer from solubility issues. The partial hydrophobic nature of these multimodal imaging agents reduces the surrounding water contents around the MRI probe, resulting in attenuated MRI signals [88]. Secondly, the conjugation and preservation of the fluorescence moiety prefers alkaline condition, which is not favorable for Gd^{3+} chelate formation [89]. And most importantly, interference can arise from limited molecular attachment points, as introduction of targeting agent can alter the affinity of receptor binding. To overcome these disadvantages, the use of various nanostructure vehicles arose to create highly loaded and multi-functional imaging probes. Riding on the advantages of nanostructure vehicles, several kinds of optical-T_1 MRI agents were developed based on mesoporous silica nanoparticles (MSNs), quantum dots (QDs), hybrid lipid micelles, chitosan, dendrymeric nanoparticle etc.

4.1.1. Silica nanoparticle in Optical/T_1 imaging—MSN with well defined morphology and porosity may be used to develop various kinds of hybrid nanostructures. It is well established that this genre of nanoparticles posses great stability in a wide range of

thermal and chemical-biological conditions. The MSNs also have external and internal surfaces that can be selectively functionalized with different organic and inorganic groups though conventional chemistry [90].

In regards to (*in vivo*) biological application, MSNs are highly biocompatible, and show efficient uptake by living cells and controlled release of drugs [91]. Considering the above advantages, MSNs have attracted research in the development of optical-MRI hybrid nanomaterials. In one of the most representative works, Wenbin *et al.*, not only combined luminescent complex with T_1 MRI agents, but also added FITC as a fluorescent probe in MSN [92, 93]. In their model, silica nanoparticles were first doped with luminescent $[Ru(bpy)_3]Cl_2$ by Stober's sol-gel method, then Gd-Si-DTTA (gadolinium (trimethoxysilylpropyl) diethylenetriaminetetraacetate) or Gd-Si-DTPA (gadolinium bis(triethoxysilylpropyl) diethylenetriaminepentaacetate) was added to form a layer of gadolinium doped silica shell. The inner core served as an optical imaging agent, and the outer shell operated as a T_1 and T_2 weighted MR imaging agent (Figure 5A, B). The two different silane ligands were used to increase the payload of Gd ion. Although they are able to increase the payload of Gd ions by six times, the relaxivity did not increase proportionally. They observed $R_1 = 4.9 \times 10^5$ and $R_2 = 7.8 \times 10^5$ s^{-1} per millimolar particles in compare to $R_1 = 2.0 \times 10^5$ and $R_2 = 6.1 \times 105$ s^{-1} per millimolar particles for Gd-DTPA and Gd-DTTP, respectively. Although proportional increase in R_1 was not observed, the relaxivity values in both cases were higher than individual gadolinium complexes. This effect was ascribed to slow tumbling caused by the Gd chelate being fixed to a higher molecular structure. However, higher relaxivity was not achieved because the water molecules could not access the inner Gd doped silica layers to generate additional MRI signals.

The efficacy of these dual modal nanohybrids was tested *in vitro* using monocyte cell lines. This cell line was efficiently labeled with these nanohybrids and successfully imaged by optical and MR techniques (Figure 5C). Following this report, the work was extended to include dye doped silica nanoparticles for cancer specific multimodal imaging [93]. In this follow-up, the previously reported Gd-nanohybrids were additionally functionalized with fluorescein isothiocyanate (FITC) using a layer-by-layer (LbL) self assembly method. HT-29 cells were successfully targeted and imaged with the new generation of particles which is electrostatically functionalized with K_7RGD peptide.

In another interesting application, Schooneveld *et al.* successfully used silica coated gold nanaoparticles as a vehicle for fluorescent and paramagnetic agents. This hybrid imaging agent not only served as an optical and MRI agent, but also as an X-ray computed tomography (CT) probe [94]. This work demonstrated trimodal imaging of macrophage cells *in vitro* and mice livers *in vivo* via T_1 weighted MRI, CT and fluorescence imaging. Similarly, Gerion *et al.* [95] reported silica coated quantum dots covalently linked to Gd^{3+} ions chelator for optical-MR imaging. Here, the silica coated CdSe/ZnS QDs were first prepared by mercaptopropyltrimethoxysilane (MPS) polymerization of siloxane then covalently attached with multiple paramagnetic gadolinium chelate, gadolinium-tetraazacyclododecanetetraacetic acid (Gd-DOTA). This nanohybrid not only shows potentiality as an imaging agent, but also has very minimal health effects on animals. In a preliminary study on mice, it was revealed that this silica-coated optical/MRI probes are cleared from the renal system into the bladder with no observable side effects.

4.1.2. Quantum Dots in Optical/T_1 imaging—A fluorescent alternative to organic fluorophores are semiconducting nanoparticles that exhibit bright fluorescence and photostability, called Quantum Dots (QDs). Considering their unique optical property, QDs have been a popular imaging device in biology since its invention [96, 97]. Similar to other

nanomaterials, QDs can be conjugated, doped or coated with other materials, as Gerion *et al.* did [95], to provide MR imaging capabilities. Because QDs can offer reactive surface functionalities, a large number of paramagnetic ion containing chelates can be accommodated on its surface. Although initially there were are issues regarding the stability and toxicity of QDs for *in vitro* and *in vivo* applications, several methods have since developed to minimize those limitations. Like other materials, paramagnetic ion or chelate can be doped into or conjugated with QDs, and as was demonstrated in the previous example, T_1 agents can be attached with other coating agents.

The first strategy to prepare QD based dual mode MRI agent was based on conjugation of carboxylate stabilized QDs with commercially available NHS esters of DOTA and DTPA [98, 99]. Following those initial reports, QDs with MRI contrast abilities began surfacing in literature. Many, unfortunately, suffered from limited light emission or low MRI contrast [100, 101]. These limitations were overcome in a report by Jin *et al.*, where glutathione stabilized NIR fluorescence CdSeTe/CdS ODs were used to conjugate Gd^{3+}-DOTA ligands [12]. This nanohybrids showed a seven fold increase in fluorescence over indocyanine green (ICG). Similarly, extremely favorable MR properties were also observed: 365 mM^{-1} s^{-1} for R_1 relaxivity and 6779 mM^{-1} s^{-1} for R_2. Using these magnetic nanostructures, they were able to perform *in vivo* fluorescence and MRI imaging using mouse models (Figure 6A, B). Use of dendrimers can also increase gadolinium loading on QDs. Prinzen *et al.* developed QD-GD^{3+} based dendritic nanohybrid which allowed visualization of cell death and activated platelets using fluorescence imaging and T_1 weighted MRI [102]. To increase the MRI sensitivity, Gd-DTPA loading was increased by using biotinylated lysine wedges with eight Gd-DTPA complexes attached to its periphery. In addition, Annexin A5 (AnxA5), a well-explored molecular imaging probe [103], was also attached to visualize cell surface exposure of phosphatidylserine (PS). These particles exhibited intense fluorescence and a large R_1 relaxivity of 3000–4500 mM^{-1} s^{-1}, which compares favorably to the 420–630 mM^{-1}s^{-1} for non dendrimeric Gd-DTPA conjugated nanoparticles. The QD synthesis study was accompanied by *in vitro* study using PS exposed with activated platelets. They also demonstrate specific targeting capability by using the murine carotid artery as the targeted organ.

In another example, a bimodal, multivalent contrast agent was prepared with high loading of paramagnetic ion using streptavidin conjugated QDs and biotin terminated polylysine dentitic wedges (Figure 6D) [104]. According to the report, each QD carried a maximum of 192 Gd ions with six cyclic Asn-Gly-Arg (cNGR) peptides. cNGR was used for molecular imaging of angiogenesis which binds specifically to the $\alpha_v\beta_3$-integrin. The T_1 relaxivity of cNGR-Gd-QDs per Gd ion, was 7.1 ± 0.4 mmol/L^{-1}s^{-1} at 7 T and 20°C, which lies in the expected range for macromolecular contrast agents.

Another popular method to prepare QD-Gd structures is through liposomal encapsulation. In this method two or more types of contrast agents are trapped in a micelle. In case of QD encapsulation, Gd chelate containing lipids are used to initiate the liposome formation. A wide variety of constructs using this platform was reported by Mulder's research group, where they mixed QDs with a range of modified lipids to prepare bimodal imaging agents [105–107]. In a typical preparation method, TOPO/HDA (trioctylphosphineoxide/ hexadecylamine) coated QDs were mixed with PEG-DSPE (1,2-distearoyl-sn-glycero-3-phosphoethanolamine-*N*-[methoxy(poly(ethylene glycol))-2000]), and a paramagnetic lipid, Gd-DTPA-BSA (Gd-DTPA-bis(stearylamide) in organic solvent. Here, PEG-DSPE was used to stabilize the liposome and enhance biocompatibility while Gd-DTPA-BSA was used as the MRI agent. After the mixing, the organic solvent was evaporated, followed by rehydration in HEPES buffer. Subsequently, specific targeting ligands were introduced. In one example, cyclic RGD peptide was conjugated with these nanohybrids to image activated

and angiogenic vascular endothelium [108]. The lysine residue of the peptide was first modified with thiol, then react with maleimide-functionalized PEG lipids present in the micellular coat (Figure 7A). The potentiality of targeted multimodal imaging of tumor angiogenesis was demonstrated on mice [106]. The nanohybrids were intravenously injected and studied *in vivo* with fluorescence imaging and MRI. Additionally, the fate of injected multimodal imaging agent were monitored in real time using intravital microscopy. As shown in figure 7B,C, the fluorescence imaging enabled the visualization of particle accumulation with high sensitivity. T_1-weighted MRI was performed in a similar condition to optical measurement and revealed significant signal enhancement that was mainly found at the tumor periphery (Figure 7D).

It is also possible to incorporate of paramagnetic ion directly in to the QD. This has been a less popular approach. Thus far, Mn doped CdS/ZnS core/shell QD is the only successful report [109]. This nanohybrid was injecxted to a rat carotid artery for multimodal imaging. Because the paramagnetic ions in this case is embedded within the QD, we imagine that access of water molecules to the paramagnetic ions can be problematic (similar to silica shells). QD luminescence can be reduced due to introduction of dopants.

4.1.3. Other Optical/T_1 imaging agent—Other than silica and QD, the most reported optical-T_1 dual imaging nanohybrids are based on lipid and dendrimeric nanoparticle. In the above discussion, Mulder group used QD as an optical imaging agent, where other fluorophore can also be trapped with paramagnetic ion to use as a multimodal imaging agent. Bimodal Optical/T_1 lipid nanoparticles consist of lipid functionalized with Gd chelate and fluorescent molecule. The most common bimodal lipids are a combination of either Gd or Mn chelate with rhodamine as a fluorophore (Gd/Mn-Rh-Lipid NP) [110–113]. Gd-Rh-Lipid NP was applied *in vivo* for tracking tumor cells at cellular scale by optical imaging in addition to anatomical information from T_1 weighted MRI. In a representative example, macrophage cells were treated with variable ratio of paramagnetic ion and fluorophore containing lipids to get optimum multimodal imaging [113]. In that study Gd-DTPA-DSA, a Gd^{3+} chelating lipid which exhibits paramagnetic properties for MRI, and P2fA2, a fluorescein labeled apolipoprotein E derived lipopeptide, were mixed in different ratio to obtain tunable size, contrast and cellular uptake (Figure 8A). Based on their correlation study, the most suitable compositions are 33 and 50 mol% of P2fA2, as they have small size and the high relaxivity. These two lipid nanohybrid were applied to cultured mouse macrophage cells (J774A1) for *in vitro* experiments. The intake was successfully visualized using fluorescence confocal laser scanning microscopy and MRI (Figure 8B,C,D).

Another way to prepare optical/T1 bimodal lipid nanohybrid is by combining florescent lanthanides (e.g. Eu^{3+}, Tb^{3+}, Dy^{3+} etc.) with Gd^{3+} [114–116]. By using this construct, it is very convenient to control the two lanthanide ions using the same chelating ligand. As the required concentration of Gd^{3+} ions is always higher than the fluorescent components, the initial ratios of two lanthanides can be used to optimize the relative sensitivity.

In comparison to doping, assembly and encapsulation, dendrimeric nanoparticles are also potential platforms for multimodal imaging. The PAMAM dendrimers, which are considered very biocompatible, are brunched polymer terminated with large number of amines. The branched nature of the dendrimeric material can offer large number of functional group at very small particle size [117]. The surface amine group of PAMAM dendrimer was functionalized with DTPA, a Gd^{3+} chelate, and various optical dyes to prepare bimodal imaging agent [118]. So far rhodamine [119], rhodamine green [85], Alexa Fluor [120] and Cy5.5 [121] fluorescent dyes were incorporated with Gd-DTPA. Although the dedrimers are not easy to synthesize, their recent commercial availability make it a potential platform for multimodal imaging.

4.2. Optical-T_2 MRI agent nanohybrids

Iron based MNS are most typically used as T_2 contrast agents. They typically exhibit higher relaxivities values compared to T_1 agents, and can be used at lower dosages. Like other nanoparticle agents, iron based MNSs are popular multimodal imaging vehicles. Here, surface conjugation with alternative imaging probes is the most studied methodology for creating multimodal agents.

4.2.1. Fluorophore conjugated MNSs as optical/T_2 nanohybrid—MNSs have been coupled with a wide range of fluorophores for T_2/Optical imaging applications and optically monitored magnetic separation assays. Through surface conjugation, the following fluorophores have been successfully applied to MNS systems: rhodamines, cyanines (Cy5.5, Cy7.5), AlexaFluors, dansyl, indolequinone and fluorescein. To enable surface conjugation, MNSs particles were typically coated with amphiphilic polymer, surfactant, silaen PEG, and amine terminated PEG or dextran with amine or carboxylate as a terminal group. In most of the references the conjugation procedures are not well described, with the exception of the protocol reported by Weissleder group in *Nature Protocol, 2006* [122].

Although there are several reports on fluorophore conjugated MNSs used as bimodal imaging agents where the fluorescence and MR signal coexist, there are also some reports of fluorescence quenching when iron oxide nanostructures were used as fluorophore vehicles. This quenching was observed in case of Cy5.5, Cy7 (two red shifted cyanine fluorophores), doxorubicin, Suwannee River fulvic acid etc, when fluorophores were covalently or noncovalently attached to the iron oxide MNSs [123–125]. While there was no clear explanation for the origin of quenching, the phenomenon has been used for monitoring drug delivery and in protease sensing. In the report, Cy7 was conjugated to an amine functional iron oxide nanoparticle in a protease resistant manner, while simultaneously attaching Cy5.5 to a protease sensitive polyarginine peptide spacer. When attached to the MNS, the fluorescence of both were quenched, but in the presence of protease the fluorescence of Cy5.5 was recovered [125]. Even with the reported quenching effects, there were demonstrated successes in fluorescent imaging of iron oxide conjugated fluorophores present in literature.

One popular MNS, a Cy5.5-iron oxide nanohybrids, was used for target specific optical and T_2 weighted bimodal imaging. Perhaps the most renowned applications were reported by Weissleder, Josephson and their collaborators. In a recent example, *in vivo* imaging of cardiomyocyte apoptosis and necrosis were performed within 4 to 6 hours of injury using annexin-based dual mode MNS probes (AnxMNS-Cy5.5) [126]. Sosnovik *et al.* found the uptake of AnxMNS-Cy5.5 was most prominent in the midmyocardium and was significantly greater than without annexine (contrast-to-noise ratio, 8.82 ± 1.5 vs. 3.78 ± 1.1; *P*<0.05) [127]. Another advantage of the nanoparticulate structure of T_2 agent can be used by conjugating fluorescent antibodies to the surface of MNS for target-specific optical/T_2 dual mode imaging.

Similar to small molecules, QDs can also attach directly to MNS to construct dual mode imaging nanohybrids. In one example, CdSe/ZnS QD was coupled with polymer coated MNS by using thiol chemistry. [128]. This probe was used for optical imaging and separation of MCF-7 breast cancer cells from serum solutions by immobilizing anticycline E antibodies on nanohybrids surface. The magnetic property of this nanohybrid also suggests the possible application in T_2 MRI.

4.2.2. Silica based MNSs as optical/T_2 nanohybrid—Silica based construction of multimodal imaging agents are very popular in medicinal science due to several advantages such as amorphous structure (enable large loading), water solubility, biocompatibility and

easy surface modification for conjugation. As discussed in previous sections, optical/T_2 nanohybrid with silica and MNS can be synthesized in several ways. The most convenient of which include, (i) trapping the fluorophore in a mesoporous silica shell with the core MNSs, [12] conjugation of dyes with silica shell surface and (iii) using silica particles as the main nanoparticle vehicle to carry MNS and fluorophores (Figure 9).

A wide array of dyes can be entrapped in a silica shell by using modified Stober methods. In most reported methods, the magnetic core is first coated with a thin layer of silica. Subsequently, a follow-up layer of silica is formed using a solution of tetraethylorthosilicate (TEOS) mixed with fluorophores, creating a second silica coating with fluorescent properties. The loading of dye molecule can be tuned by controlling the thickness of the silica shell. There are reports using dye-coupled silica precursors and the reverse micelle process to create fluorescent MNS hybrids. So far, a wide range of fluorophore have been used, ranging from small molecule (FITC, rhodamine etc.), inorganic luminescent complex (terbium complex) to polymer and QDs. In a recent report by Chen *et al.* [129] magnetic iron oxide/silica nanocomposites were modified with fluorescent polymethacrylic acid for cancer targeting. The nanocomposite, with $\lambda_{ex} = 475$ nm and $\lambda_{em} = 592$ nm also demonstrated room temperature magnetic saturation of 31.2 emu g^{-1}. This 280nm nanohybrid shows an excellent drug-loading efficiency (105.8 mg of drug/mg of drug carrier) and 85 % favorable biocompatibility with suitable dispersibility under physiological conditions. Dyes were incorporated by using standard conjugation chemistry after initial silica shell formation around MNSs. Alternatively the inorganic complexes, such as metal ions, can be connected to a primary vehicle through conjugation of chelating ligand, as discussed in the T1/Optical nanohybrids section. In one example, terbium was introduced using DTPA-derivatized silane precursor, which can be used for bio-imaging, bio-labeling and bioassays because as they track with an external magnetic field and exhibit unique phosphorescence properties [130]. It is also possible to prepare a silica based bimodal imaging agent using mesoporous dye-doped silica nanoparticles as the core. In this case, magnetic MNSs were subsequently immobilized on the surface of the silica. This method was used by the Hyeon group to fabricate their dual-mode nanohybrids [131]. Here, rhodamine B or fluorescein doped amine functionalized silica nanoparticle were completed with Fe_3O_4 iron oxide nanoparticles to form assemblies for simultaneous MRI, fluorescence imaging. They also used this nanohybrid as a drug delivery vehicle by loading the anticancer drug molecule into the pores of mesoporous silica nanoparticles (Figure 10A).

Due to their close proximity and water exposure, the MNSs assembled on the silica surface demonstrated synergistic magnetic properties that enhanced MR signals. The R_2 of free Fe_3O_4 nanocrystals was 26.8 mM^{-1} s^{-1} at 1.5 T, while the nanohybrids exhibit higher relaxivity value of 76.2 mM^{-1} s^{-1}. Probable explanation for this enhancement is mainly due to the assembly of multiple MNS on silica surface. Because these structures were dye doped and further stabilized by PEG (emission peak at 520 nm and 576 nm, typical for fluorescein and rhodamine B), they are applicable for biological multi-modal imaging. To demonstrate this capability, fluorescence and T_2 weighted MR images of phantom cells were measured simultaneously. As the concentration of nanohybrids was increased the fluorescence signal was increased and the T_2 weighted image was darkened (Figure 10B,C).

4.2.3. Hybrid Micelles and Other optical/T_2 nanohybrid—As we described above in the optical/T_1 nanohybrid section, the preparation and advantage of liposomal encapsulation can also be applied for MNSs. As it is possible to encapsulate multiple imaging agents in the same liposome, MNSs can be encapsulated with various optical probes. Using this method, iron oxide MNS entrapped in the same liposome as QDs has been reported [132–134]. The sizes of these nanohybrids range from 25 nm to 70 nm depending on the amphiphiles used. For example, when PEGylated phospholipid was used to trap the QD and iron oxide

nanostructure, 60–70 nm diameter micelles were formed [133]. On the other hand, 25 nm hybrid micelles were prepared by using PEGylated gallate amphiphiles [134]. By controlling the relative concentration of QD and MNS, Park *et al.* prepared a range of nanohybrids with R_2 relaxivity ranging from 103.9 to 244.9 mM^{-1} s^{-1}, depending on iron concentration. The nanohybrids can be assembled with not only with QDs and MNSs but also with the anticancer drug doxorubicin and targeting peptide F3. Using these multimodal nanohybrids they successfully target, deliver and dual mode image the tumor tissues.

Chitosan is a linear positively charged polysaccharide composed of arbitrarily distributed D-glucosamine and N-acetyl-D-glucosamine. It has a number of potential biomedical uses due to its high biocompatibility. Furthermore, its ability to electrostatically bind proteins and internalize them in to cells allows it to cross the blood–brain barrier. By applying their interactive properties, MNS and fluorophores can be combined together for bimodal imaging [135]. Based on the reported articles, MNS-FITC [136] and MNS-QD [137] can be prepared as nanohybrids using chitosan. There are two ways in which the chitosan composite can be prepared, through a "step by step" method, or a "simultaneously" method. In the step by step method, MNS or QD (as fluorophore) are first electrostatically adsorbed into chitosan polymer and then coated to produce a chitosan-hybrid matrix. Other imaging agent can be attached subsequently. In the simultaneous method, all imaging agents are mixed with chitosan to form a nanohybrid. In the latter method, the size of the nanohybrids are comparatively small (~50 nm), allowing better imaging in biological applications. The chitosan based T_1 imaging agents are not very popular, due to the leaching of Gd^{3+} [138], which is not observed in the case of MNSs. Although chitosan nanohybrids do not release larger particles in its matrix (eg MNSs, QDs), its high porosity can easily release the entrapped small molecules. This can be useful in drug delivery application with multimodal imaging.

Different from all of the above methods in preparation of optical/T_2 bimodal imaging agent, is the doping of MNSs with luminescent ions. There are very few reports on this kind of imaging agent. In a work, reported by Zhang *et al.*, terbium was doped in iron oxide nanoparticles [139]. The nanohybrid was prepared by high temperature simultaneous decomposition of corresponding metal-oleate complexes. Then these nanohybrids are coated with ZnS and stabilized in working media by silica based amine functionalization [140]. The final nanohybrids are 13 nm in size, λ_{ex} = 235 nm, λ_{em} = 545 nm and superparamagnetic in nature.

4.3. T_1–T_2 MRI nanohybrids

From the all studies above we can see that T_1 weighted images with paramagnetic materials, such as gadolinium ion (Gd^{3+}) and manganese ion (Mn^{2+}), provide bright "positive contrast" (T_1) while T_2 weighted images with superparamagnetic nanoparticles (MNSs) produce dark contrast (T_2). Even though both MRI techniques are powerful and fairly noninvasive diagnostic techniques, single mode contrast agents are not sufficient for all situations as they have certain limitations. For instance, the dark contrast produced by T_2 agents can also be generated from adjacent bones or vasculatures [141]. Additionally, susceptibility artifacts can also occur as a result of the sharp change in magnetic field surrounding the contrast agent, resulting in distorted anatomy [142]. Therefore, depending on the tissue and site of interest, complementary T_1/T_2 weighted MRI imaging may facilitate improved diagnosis. Anatomic information may also be sharpened in the image. Although this is a very promising hybrid system, there are still very few reports in literature [143–145]. From various reports, it was shown that ultrasmall iron oxide MNS shows T_1 contrast effect, but due to the small superparamagnetic domain, the T_2 contrast is very low [146]. Additionally, there is little control over the T_1 vs T_2 ratio. To improve this performance, several alternate schemes have been produced to generate better T_1/T_2 dual mode contrast

agents. Among the reported T_1/T_2 nanohybrids, the most attractive systems are, (i) liposom based nanohybrids, which is the combination of MNS and paramagnetic ion, magnetic/ graphite – core-shell nanostructure and (iii) direct conjugation of paramagnetic ion with superparamagnetic nanostructure.

Phospholipid based magnetoliposomes were typically prepared by first mixing appropriate amount of lipid components in chloroform followed by evaporation. The liposomes were then mixed with lauric acid stabilized iron oxide nanoparticle to yield the final product. The resulting nanohybrid can be loaded with gadolinium ion, to constract the T_1/T_2 bimodal MRI agent. In an interesting report, Gd^{3+} ions were conjugated at the surface of both the inner and outer bilayer shells of the magnetoliposome [147]. The loading of Gd^{3+} by PE-DTPA chilate was monitored by colorimetric method using Arsenazo dye. They were also able to tune the loading Gd^{3+} using various combinations of multiple phospholipids and the best combination for highest Gd^{3+} payload per magnetoliposome was achieved by DMPC/ DMPG/DMPE-DTPA mixing ratio of 0.9:0.1:1.0. The resulting nanohybrids can have great potential in MRI, although no imaging was done by the authors.

Another very interesting T_1/T_2 agent was reported by Seo *et al.* [50], when using FeCo/ graphite-shell nanocrystals. Although the origin of this dual behavior is not completely understood, the unique imaging properties of this nanohybrid attracted a lot of attention. FeCo/single graphite shell nanohybrid was prepared by scalable chemical vapor deposition on silica, followed by etching the silica by HF. Due to the graphite coating, this nanomaterial exhibit supreme stability against oxidation and leaching. Also this nanohybrid showed superparamagnetic behavior at room temperature with saturation magnetization value of 215 e.m.u. g^{-1} (the size of the nanohybrid was 7 nm). For MRI measurement FeCo/ graphite shell nanohybrid was stabilized in aqueous solution by noncovalent functionalization with phospholipid-polyethylene glycol (Figure 11A). The observed T_1 and T_2 relaxivities r_1 and r_2 with 7nm and 4nm FeCo/graphite shell nanoparticle was compared to commercially available Feridex and Magnevist MR contrast agent under 1.5 T MRI. The R_2 value for 7 nm composite showed an approximate six fold increase over Feridex, and at 644 mM^{-1} s^{-1}, it was the highest R_2 value ever reported. This nanohybrid also exhibited a very high R_1 value (70 mM^{-1} s^{-1}), opening the possibility of using this material as a positive and negative MRI contrast agent (Figure 11B). The biological application was also explored by labeling the mesenchymal stem cell and *in vivo* intravascular MRI of the blood pool in the rabbit.

Lastly, T_1/T_2 MRI agent can also be prepared by directly conjugating/absorbing T_1 chelating agent on the MNS surface. The difficulty associated with this kind of design arises from close proximity of T_1 and T_2 agent. When the T_1 agent are connected with superparamagnetic MNS in close proximity, the induced magnetic field generated by a superparamagnetic MNS (T_2) material will interfere with the relaxation process of the paramagnetic T_1 contrast agent (Figure 12A). This undesirable effect reduces the T_1 signal significantly. To understand the effect of distance between the MNS core and the T_1 agent, Choi *et al.* recently reported a T_1/T_2 hybrid with T_1 and T_2 agents separated by a magnetically decoupling silica shell [148]. The T_2 core material, a 15 nm $MnFe_2O_4$ MNS, was coated with varying SiO_2 shell thicknesses (4, 8, 12, 16, and 20 nm) and then $Gd_2O(CO_3)_2$, the T_1 contrast agent, was absorbed on a silica layer using a $Gd(NO_3)_3$ precursor. The T_1 and T_2 versus SiO_2 shell thickness are shown in figure 12C. According to their report, this behavior originated from distance dependent magnetic coupling between T_1 and T_2 agent. In a separate report, gadolinium chelates were directly anchor on the surface of the iron oxide nanoparticle using Dopamine to create a T_1/T_2 bimodal MRI agent [149]. The observed MR values, recorded using a 3T scanner, showed the r_2 values decreased from

225.81 to 30.32 mM^{-1} s^{-1} after the conjugation with gadolinium chelates. The R$_1$ value was 11.17 mM^{-1} s^{-1}.

5. Summary and Conclusions

By synergizing elements of chemistry, material science and biomedical engineering, many nanoscale MR probes have been developed within the past decade. With this rapid advancement, new diagnostic and theranostic approaches have emerged. We attempted to cover a portion of these developments by focusing on T$_2$ and multimodal agents with optical, T$_1$ and T$_2$ functionalities. Specifically, we covered the synthesis, surface functionalization and stabilization of MR agents, coupling to optical and/or other MR agents and applications *in vitro* and *in vivo*.

These new MR agents, especially those with multi-modal capabilities, are expected to provide exquisite sensitivity and specificity in tracking molecular and cellular processes. Although many of these promises have been realized in the academic settings, significant hurdles still exist in translating these results in to clinical therapy. To overcome these issues, problems ranging from cost, synthesis scale and human compatibility will have to be surmounted. These are not because these challenges are not unique to MR agents, it is expected that they are surmountable in the near future.

Cited References

1. Brenner DJ, Hall EJ. Current concepts - Computed tomography - An increasing source of radiation exposure. New England Journal of Medicine. 2007; 357:2277–2284. [PubMed: 18046031]

2. Basu S, Chryssikos T, Moghadam-Kia S, Zhuang HM, Torigian DA, Alavi A. Positron Emission Tomography as a Diagnostic Tool in Infection: Present Role and Future Possibilities. Seminars in Nuclear Medicine. 2009; 39:36–51. [PubMed: 19038599]

3. Meerwaldt R, Slart RHJA, van Dam GM, Luijckx GJ, Tio RA, Zeebregts CJ. PET/SPECT imaging: From carotid vulnerability to brain viability. European Journal of Radiology. 2010; 74:104–109. [PubMed: 19246168]

4. Hong R, Fischer NO, Emrick T, Rotello VM. Surface PEGylation and Ligand Exchange Chemistry of FePt Nanoparticles for Biological Applications. Chemistry of Materials. 2005; 17:4617–4621.

5. Heeger DJ, Ress D. What does fMRI tell us about neuronal activity? Nature Reviews Neuroscience. 2002; 3:142–151.

6. Francois CJ, Schiebler ML, Reeder SB. Cardiac MRI Evaluation of Nonischemic Cardiomyopathies. Journal of Magnetic Resonance Imaging. 2010; 31:518–530. [PubMed: 20187194]

7. Seevinck PR, Deddens LH, Dijkhuizen RM. Magnetic resonance imaging of brain angiogenesis after stroke. Angiogenesis. 2010; 13:101–111. [PubMed: 20552268]

8. Caravan P, Ellison JJ, McMurry TJ, Lauffer RB. Gadolinium(III) chelates as MRI contrast agents: Structure, dynamics, and applications. Chemical Reviews. 1999; 99:2293–2352. [PubMed: 11749483]

9. De M, Ghosh PS, Rotello VM. Applications of Nanoparticles in Biology. Advanced Materials. 2008; 20:4225–4241.

10. Jennings LE, Long NJ. 'Two is better than one'-probes for dual-modality molecular imaging. Chemical Communications. 2009:3511–3524. [PubMed: 19521594]

11. Louie A. Multimodality Imaging Probes: Design and Challenges. Chemical Reviews. 2010; 110:3146–3195. [PubMed: 20225900]

12. Jin T, Yoshioka Y, Fujii F, Komai Y, Seki J, Seiyama A. Gd3+-functionalized near-infrared quantum dots for in vivo dual modal (fluorescence/magnetic resonance) imaging. Chemical Communications. 2008:5764–5766. [PubMed: 19009074]

13. Kobayashi Y, Imai J, Nagao D, Takeda M, Ohuchi N, Kasuya A, Konno M. Preparation of multilayered silica-Gd-silica core-shell particles and their magnetic resonance images. Colloids and Surfaces a-Physicochemical and Engineering Aspects. 2007; 308:14–19.

14. Xu JJ, Ao YH, Fu DG, Yuan CW. Synthesis of Gd-doped TiO2 nanoparticles under mild condition and their photocatalytic activity. Colloids and Surfaces a-Physicochemical and Engineering Aspects. 2009; 334:107–111.

15. Song Y, Xu XY, MacRenaris KW, Zhang XQ, Mirkin CA, Meade TJ. Multimodal Gadolinium-Enriched DNA-Gold Nanoparticle Conjugates for Cellular Imaging. Angewandte Chemie-International Edition. 2009; 48:9143–9147.

16. Kobayashi H, Brechbiel MW. Nano-sized MRI contrast agents with dendrimer cores. Advanced Drug Delivery Reviews. 2005; 57:2271–2286. [PubMed: 16290152]

17. Manus LM, Mastarone DJ, Waters EA, Zhang XQ, Schultz-Sikma EA, MacRenaris KW, Ho D, Meade TJ. Gd(III)-Nanodiamond Conjugates for MRI Contrast Enhancement. Nano Letters. 2010; 10:484–489. [PubMed: 20038088]

18. Sitharaman B, Van Der Zande M, Ananta JS, Shi XF, Veltien A, Walboomers XF, Wilson LJ, Mikos AG, Heerschap A, Jansen JA. Magnetic resonance imaging studies on gadonanotube-reinforced biodegradable polymer nanocomposites. Journal of Biomedical Materials Research Part A. 2010; 93A:1454–1462. [PubMed: 19927368]

19. Endres PJ, Paunesku T, Vogt S, Meade TJ, Woloschak GE. DNA-TiO2 nanoconjugates labeled with magnetic resonance contrast agents. Journal of the American Chemical Society. 2007; 129:15760–15761. [PubMed: 18047347]

20. Major JL, Meade TJ. Bioresponsive, Cell-Penetrating, and Multimeric MR Contrast Agents. Accounts of Chemical Research. 2009; 42:893–903. [PubMed: 19537782]

21. Hu F, Joshi HM, Dravid VP, Meade TJ. High-performance nanostructured MR contrast probes. Nanoscale. 2010; 2:1884–1891. [PubMed: 20694208]

22. Modo MMJ, Bulte JWM, Kim EE. Molecular and Cellular MR Imaging. J Nucl Med. 2007; 48:2087.

23. Roch A, Gossuin Y, Muller RN, Gillis P. Superparamagnetic colloid suspensions: Water magnetic relaxation and clustering. Journal of Magnetism and Magnetic Materials. 2005; 293:532–539.

24. Perez JM, Josephson L, O'Loughlin T, Hogemann D, Weissleder R. Magnetic relaxation switches capable of sensing molecular interactions. Nat Biotech. 2002; 20:816–820.

25. Perez JM, O'Loughin T, Simeone FJ, Weissleder R, Josephson L. DNA-Based Magnetic Nanoparticle Assembly Acts as a Magnetic Relaxation Nanoswitch Allowing Screening of DNA-Cleaving Agents. Journal of the American Chemical Society. 2002; 124:2856–2857. [PubMed: 11902860]

26. Hu F, MacRenaris KW, Waters EA, Schultz-Sikma EA, Eckermann AL, Meade TJ. Highly dispersible, superparamagnetic magnetite nanoflowers for magnetic resonance imaging. Chemical Communications. 2010; 46:73–75. [PubMed: 20024297]

27. Barick KC, Aslam M, Prasad PV, Dravid VP, Bahadur D. Nanoscale assembly of amine-functionalized colloidal iron oxide. Journal of Magnetism and Magnetic Materials. 2009; 321:1529–1532. [PubMed: 20160860]

28. Jun, Y-w; Huh, Y-M.; Choi, J-s; Lee, J-H.; Song, H-T.; KimKim; Yoon, S.; Kim, K-S.; Shin, J-S.; Suh, J-S.; Cheon, J. Nanoscale Size Effect of Magnetic Nanocrystals and Their Utilization for Cancer Diagnosis via Magnetic Resonance Imaging. Journal of the American Chemical Society. 2005; 127:5732–5733. [PubMed: 15839639]

29. Morales MP, Veintemillas-Verdaguer S, Montero MI, Serna CJ, Roig A, Casas L, Martinez B, Sandiumenge F. Surface and Internal Spin Canting in γ-Fe2O3 Nanoparticles. Chemistry of Materials. 1999; 11:3058–3064.

30. Joshi HM, Lin YP, Aslam M, Prasad PV, Schultz-Sikma EA, Edelman R, Meade T, Dravid VP. Effects of Shape and Size of Cobalt Ferrite Nanostructures on Their MRI Contrast and Thermal Activation. The Journal of Physical Chemistry C. 2009; 113:17761–17767.

31. Lee J-H, Huh Y-M, Jun Y-w, Seo J-w, Jang J-t, Song H-T, Kim S, Cho E-J, Yoon H-G, Suh J-S, Cheon J. Artificially engineered magnetic nanoparticles for ultra-sensitive molecular imaging. Nat Med. 2007; 13:95–99. [PubMed: 17187073]

32. Pinho SLC, Pereira GA, Voisin P, Kassem J, Bouchaud Vr, Etienne L, Peters JA, Carlos L, Mornet Sp, Geraldes CFGC, Rocha Jo, Delville M-Hln. Fine Tuning of the Relaxometry of γ-Fe2O3@SiO2 Nanoparticles by Tweaking the Silica Coating Thickness. ACS Nano. 2010; 4:5339–5349. [PubMed: 20795638]

33. Lu Y, Yin Y, Mayers BT, Xia Y. Modifying the Surface Properties of Superparamagnetic Iron Oxide Nanoparticles through A Sol–Gel Approach. Nano Letters. 2002; 2:183–186.

34. Ennas G, Musinu A, Piccaluga G, Zedda D, Gatteschi D, Sangregorio C, Stanger JL, Concas G, Spano G. Characterization of Iron Oxide Nanoparticles in an Fe2O3–SiO2 Composite Prepared by a Sol–Gel Method. Chemistry of Materials. 1998; 10:495–502.

35. Ma D, Veres T, Clime L, Normandin F, Guan J, Kingston D, Simard B. Superparamagnetic FexOy@SiO2 Core–Shell Nanostructures: Controlled Synthesis and Magnetic Characterization. The Journal of Physical Chemistry C. 2007; 111:1999–2007.

36. Tartaj P, González-Carreño T, Serna CJ. Synthesis of Nanomagnets Dispersed in Colloidal Silica Cages with Applications in Chemical Separation. Langmuir. 2002; 18:4556–4558.

37. Liu Q, Xu Z, Finch JA, Egerton R. A Novel Two-Step Silica-Coating Process for Engineering Magnetic Nanocomposites. Chemistry of Materials. 1998; 10:3936–3940.

38. Aslam M, Li S, Dravid VP. Controlled Synthesis and Stability of Co@SiO2 Aqueous Colloids. Journal of the American Ceramic Society. 2007; 90:950–956.

39. del Campo A, Sen T, Lellouche J-P, Bruce IJ. Multifunctional magnetite and silica-magnetite nanoparticles: Synthesis, surface activation and applications in life sciences. Journal of Magnetism and Magnetic Materials. 2005; 293:33–40.

40. Hahn PF, Stark DD, Lewis JM, Saini S, Elizondo G, Weissleder R, Fretz CJ, Ferrucci JT. First clinical trial of a new superparamagnetic iron oxide for use as an oral gastrointestinal contrast agent in MR imaging. Radiology. 1990; 175:695–700. [PubMed: 2343116]

41. Hahn PFSDD, Lewis JM, Saini S, Elizondo G, Weissleder R, Fretz CJ, Ferrucci JT. First clinical trial of a new superparamagnetic iron oxide for use as an oral gastrointestinal contrast agent in MR imaging. Radiology. 1990; 175(3):695–700. [PubMed: 2343116]

42. Johnson WK, Stoupis C, Torres GM, Rosenberg EB, Ros PR. Superparamagnetic iron oxide (SPIO) as an oral contrast agent in gastrointestinal (GI) magnetic resonance imaging (MRI): Comparison with state-of-the-art computed tomography (CT). Magnetic Resonance Imaging. 1996; 14:43–49. [PubMed: 8656989]

43. Rivera Gil P, Hühn D, del Mercato LL, Sasse D, Parak WJ. Nanopharmacy: Inorganic nanoscale devices as vectors and active compounds. Pharmacological Research. 2010; 62:115–125. [PubMed: 20097288]

44. Stöber W, Fink A, Bohn E. Controlled growth of monodisperse silica spheres in the micron size range. Journal of Colloid and Interface Science. 1968; 26:62–69.

45. Lawaczeck BHR, Frenzel T, Hasegawa M, Ito Y, Kito K, Miwa N, Tsutsui H, Vogler H, Weinmann HJ. Magnetic iron oxide particles coated with carboxydextran for parenteral administration and liver contrasting. Pre-clinical profile of SH U555A. Acta Radiology. 1997; 38:584–597.

46. Jung CW. Surface properties of superparamagnetic iron oxide MR contrast agents: Ferumoxides, ferumoxtran, ferumoxsil. Magnetic Resonance Imaging. 1995; 13:675–691. [PubMed: 8569442]

47. Li W, Tutton S, Vu AT, Pierchala L, Li BS, Lewis JM, Prasad PV, Edelman RR. First-pass contrast-enhanced magnetic resonance angiography in humans using ferumoxytol, a novel ultrasmall superparamagnetic iron oxide (USPIO)-based blood pool agent. Journal of Magnetic Resonance Imaging. 2005; 21:46–52. [PubMed: 15611942]

48. McLachlan SJ, Morris MR, Lucas MA, Fisco RA, Eakins MN, Fowler DR, Scheetz RB, Olukotun AY. Phase I clinical evaluation of a new iron oxide MR contrast agent. Journal of Magnetic Resonance Imaging. 1994; 4:301–307. [PubMed: 8061425]

49. Cai W, Wan J. Facile synthesis of superparamagnetic magnetite nanoparticles in liquid polyols. Journal of Colloid and Interface Science. 2007; 305:366–370. [PubMed: 17084856]

50. Seo WS, Lee JH, Sun XM, Suzuki Y, Mann D, Liu Z, Terashima M, Yang PC, McConnell MV, Nishimura DG, Dai HJ. FeCo/graphitic-shell nanocrystals as advanced magnetic-resonance-imaging and near-infrared agents. Nature Materials. 2006; 5:971–976.

51. Molday RS, Mackenzie D. Immunospecific ferromagnetic iron-dextran reagents for the labeling and magnetic separation of cells. Journal of Immunological Methods. 1982; 52:353–367. [PubMed: 7130710]

52. Yi-Xiang, SMHaGPK.; Wang1, J. Superparamagnetic iron oxide contrast agents: physicochemical characteristics and applications in MR imaging. European Radiology. 2001; 11:2319–2331. [PubMed: 11702180]

53. Clement O, Siauve N, Cuénod C-A, Frija G. Liver Imaging With Ferumoxides (Feridex(R)): Fundamentals, Controversies, and Practical Aspects. Topics in Magnetic Resonance Imaging. 1998; 9:167–182. [PubMed: 9621405]

54. Metz S, Bonaterra G, Rudelius M, Settles M, Rummeny EJ, Daldrup-Link HE. Capacity of human monocytes to phagocytose approved iron oxide MR contrast agents in vitro. European Radiology. 2004; 14:1851–1858. [PubMed: 15249981]

55. Carmen Bautista M, Bomati-Miguel O, del Puerto Morales M, Serna CJ, Veintemillas-Verdaguer S. Surface characterisation of dextran-coated iron oxide nanoparticles prepared by laser pyrolysis and coprecipitation. Journal of Magnetism and Magnetic Materials. 2005; 293:20–27.

56. Wunderbaldinger P, Josephson L, Weissleder R. Crosslinked Iron Oxides (CLIO): A New Platform for the Development of Targeted MR Contrast Agents. Academic Radiology. 2002; 9:S304–S306. [PubMed: 12188255]

57. Reimer P, Balzer T. Ferucarbotran (Resovist): a new clinically approved RES-specific contrast agent for contrast-enhanced MRI of the liver: properties, clinical development, and applications. European Radiology. 2003; 13:1266–1276. [PubMed: 12764641]

58. Otsuka H, Nagasaki Y, Kataoka K. PEGylated nanoparticles for biological and pharmaceutical applications. Advanced Drug Delivery Reviews. 2003; 55:403–419. [PubMed: 12628324]

59. Nativo P, Prior IA, Brust M. Uptake and Intracellular Fate of Surface-Modified Gold Nanoparticles. ACS Nano. 2008; 2:1639–1644. [PubMed: 19206367]

60. Niidome T, Yamagata M, Okamoto Y, Akiyama Y, Takahashi H, Kawano T, Katayama Y, Niidome Y. PEG-modified gold nanorods with a stealth character for in vivo applications. Journal of Controlled Release. 2006; 114:343–347. [PubMed: 16876898]

61. You CC, De M, Rotello VM. Contrasting effects of exterior and interior hydrophobic moieties in the complexation of amino acid functionalized gold clusters with alpha-chymotrypsin. Organic Letters. 2005; 7:5685–5688. [PubMed: 16321022]

62. Kohler N, Fryxell GE, Zhang M. A Bifunctional Poly(ethylene glycol) Silane Immobilized on Metallic Oxide-Based Nanoparticles for Conjugation with Cell Targeting Agents. Journal of the American Chemical Society. 2004; 126:7206–7211. [PubMed: 15186157]

63. Kim S-W, Kim S, Tracy JB, Jasanoff A, Bawendi MG. Phosphine Oxide Polymer for Water-Soluble Nanoparticles. Journal of the American Chemical Society. 2005; 127:4556–4557. [PubMed: 15796504]

64. Xu C, Xu K, Gu H, Zheng R, Liu H, Zhang X, Guo Z, Xu B. Dopamine as A Robust Anchor to Immobilize Functional Molecules on the Iron Oxide Shell of Magnetic Nanoparticles. Journal of the American Chemical Society. 2004; 126:9938–9939. [PubMed: 15303865]

65. Peng S, Wang C, Xie J, Sun S. Synthesis and Stabilization of Monodisperse Fe Nanoparticles. Journal of the American Chemical Society. 2006; 128:10676–10677. [PubMed: 16910651]

66. Xie J, Xu C, Xu Z, Hou Y, Young KL, Wang SX, Pourmand N, Sun S. Linking Hydrophilic Macromolecules to Monodisperse Magnetite (Fe3O4) Nanoparticles via Trichloro-s-triazine. Chemistry of Materials. 2006; 18:5401–5403. [PubMed: 18176627]

67. Amstad E, Gillich T, Bilecka I, Textor M, Reimhult E. Ultrastable Iron Oxide Nanoparticle Colloidal Suspensions Using Dispersants with Catechol-Derived Anchor Groups. Nano Letters. 2009; 9:4042–4048. [PubMed: 19835370]

68. Wan J, Cai W, Meng X, Liu E. Monodisperse water-soluble magnetite nanoparticles prepared by polyol process for high-performance magnetic resonance imaging. Chemical Communications. 2007:5004–5006. [PubMed: 18049734]

69. Weissleder R, Cheng HC, Bogdanova A, Bogdanov A. Magnetically labeled cells can be detected by MR imaging. Journal of Magnetic Resonance Imaging. 1997; 7:258–263. [PubMed: 9039625]

70. Yeh TC, Zhang W, Ildstad ST, Ho C. Intracellular labeling of T-cells with superparamagnetic contrast agents. Magnetic Resonance in Medicine. 1993; 30:617–625. [PubMed: 8259062]

71. Yeh TC, Zhang W, Ildstad ST, Ho C. In Vivo Dynamic MRI Tracking of Rat T-Cells Labeled with Superparamagnetic Iron-Oxide Particles. Magnetic Resonance in Medicine. 1995; 33:200–208. [PubMed: 7707910]

72. Jendelová P, Herynek V, DeCroos J, Glogarová K, Andersson B, Hájek M, Syková E. Imaging the fate of implanted bone marrow stromal cells labeled with superparamagnetic nanoparticles. Magnetic Resonance in Medicine. 2003; 50:767–776. [PubMed: 14523963]

73. Jendelová P, Herynek V, Urdzíková L, Glogarová K, Kroupová J, Andersson B, Bryja V, Burian M, Hájek M, Syková E. Magnetic resonance tracking of transplanted bone marrow and embryonic stem cells labeled by iron oxide nanoparticles in rat brain and spinal cord. Journal of Neuroscience Research. 2004; 76:232–243. [PubMed: 15048921]

74. Arbab AS, Yocum GT, Kalish H, Jordan EK, Anderson SA, Khakoo AY, Read EJ, Frank JA. Efficient magnetic cell labeling with protamine sulfate complexed to ferumoxides for cellular MRI. Blood. 2004; 104:1217–1223. [PubMed: 15100158]

75. Zhu J, Zhou L, XingWu F. Tracking Neural Stem Cells in Patients with Brain Trauma. New England Journal of Medicine. 2006; 355:2376–2378. [PubMed: 17135597]

76. Heyn C, Ronald JA, Mackenzie LT, MacDonald IC, Chambers AF, Rutt BK, Foster PJ. In vivo magnetic resonance imaging of single cells in mouse brain with optical validation. Magnetic Resonance in Medicine. 2006; 55:23–29. [PubMed: 16342157]

77. Shapiro EM, Sharer K, Skrtic S, Koretsky AP. In vivo detection of single cells by MRI. Magnetic Resonance in Medicine. 2006; 55:242–249. [PubMed: 16416426]

78. Artemov D, Mori N, Okollie B, Bhujwalla ZM. MR molecular imaging of the Her-2/neu receptor in breast cancer cells using targeted iron oxide nanoparticles. Magnetic Resonance in Medicine. 2003; 49:403–408. [PubMed: 12594741]

79. McAteer MA, Sibson NR, von zur Muhlen C, Schneider JE, Lowe AS, Warrick N, Channon KM, Anthony DC, Choudhury RP. In vivo magnetic resonance imaging of acute brain inflammation using microparticles of iron oxide. Nat Med. 2007; 13:1253–1258. [PubMed: 17891147]

80. Yigit MV, Mazumdar D, Lu Y. MRI Detection of Thrombin with Aptamer Functionalized Superparamagnetic Iron Oxide Nanoparticles. Bioconjugate Chemistry. 2008; 19:412–417. [PubMed: 18173225]

81. Pichler BJ, Wehrl HF, Kolb A, Judenhofer MS. Positron emission tomography/magnetic resonance imaging: The next generation of multimodality imaging? Seminars in Nuclear Medicine. 2008; 38:199–208. [PubMed: 18396179]

82. Catana C, Wu YB, Judenhofer MS, Qi JY, Pichler BJ, Cherry SR. Simultaneous acquisition of multislice PET and MR images: Initial results with a MR-compatible PET scanner. Journal of Nuclear Medicine. 2006; 47:1968–1976. [PubMed: 17138739]

83. Aime S, Botta M, Fasano M, Terreno E. Lanthanide(III) chelates for NMR biomedical applications. Chemical Society Reviews. 1998; 27:19–29.

84. Sturzu A, Regenboyen M, Klose U, Echner H, Gharabaghi A, Heckl S. Novel dual labelled nucleus-directed conjugates containing correct and mutant nuclear localisation sequences. European Journal of Pharmaceutical Sciences. 2008; 33:207–216. [PubMed: 18243673]

85. Xu H, Regino CAS, Koyama Y, Hama Y, Gunn AJ, Bernardo M, Kobayashi H, Choyke PL, Brechbiel MW. Preparation and preliminary evaluation of a biotin-targeted, lectin-targeted dendrimer-based probe for dual-modality magnetic resonance and fluorescence Imaging. Bioconjugate Chemistry. 2007; 18:1474–1482. [PubMed: 17711320]

86. Koullourou T, Natrajan LS, Bhavsar H, Pope SJA, Feng JH, Narvainen J, Shaw R, Scales E, Kauppinen R, Kenwright AM, Faulkner S. Synthesis and spectroscopic properties of a prototype single molecule dual Imaging agent comprising a heterobimetallic rhenium-gadolinium complex. Journal of the American Chemical Society. 2008; 130:2178–2179. [PubMed: 18220401]

87. Zhang XA, Lovejoy KS, Jasanoff A, Lippard SJ. Water-soluble porphyrins imaging platform for MM zinc sensing. Proceedings of the National Academy of Sciences of the United States of America. 2007; 104:10780–10785. [PubMed: 17578918]

88. Huber MM, Staubli AB, Kustedjo K, Gray MHB, Shih J, Fraser SE, Jacobs RE, Meade TJ. Fluorescently detectable magnetic resonance imaging agents. Bioconjugate Chemistry. 1998; 9:242–249. [PubMed: 9548540]

89. Mishra A, Pfeuffer J, Mishra R, Engelmann J, Mishra AK, Ugurbil K, Logothetis NK. A new class of Gd-based DO3A-ethylamine-derived targeted contrast agents for MR and optical imaging. Bioconjugate Chemistry. 2006; 17:773–780. [PubMed: 16704217]

90. Burns A, Ow H, Wiesner U. Fluorescent core-shell silica nanoparticles: towards "Lab on a Particle" architectures for nanobiotechnology. Chemical Society Reviews. 2006; 35:1028–1042. [PubMed: 17057833]

91. Oberdorster G, Stone V, Donaldson K. Toxicology of nanoparticles: A historical perspective. Nanotoxicology. 2007; 1:2–25.

92. Rieter WJ, Kim JS, Taylor KML, An HY, Lin WL, Tarrant T, Lin WB. Hybrid silica nanoparticles for multimodal Imaging. Angewandte Chemie-International Edition. 2007; 46:3680–3682.

93. Kim JS, Rieter WJ, Taylor KML, An H, Lin WL, Lin WB. Self-assembled hybrid nanoparticles for cancer-specific multimodal imaging. Journal of the American Chemical Society. 2007; 129:8962–8963. [PubMed: 17602632]

94. van Schooneveld MM, Cormode DP, Koole R, van Wijngaarden JT, Calcagno C, Skajaa T, Hilhorst J, 't Hart DC, Fayad ZA, Mulder WJM, Meijerink A. A fluorescent, paramagnetic and PEGylated gold/silica nanoparticle for MRI, CT and fluorescence imaging. Contrast Media & Molecular Imaging. 2010; 5:231–236. [PubMed: 20812290]

95. Gerion D, Herberg J, Bok R, Gjersing E, Ramon E, Maxwell R, Kurhanewicz J, Budinger TF, Gray JW, Shuman MA, Chen FF. Paramagnetic silica-coated nanocrystals as an advanced MRI contrast agent. Journal of Physical Chemistry C. 2007; 111:12542–12551.

96. Chan WCW, Nie SM. Quantum dot bioconjugates for ultrasensitive nonisotopic detection. Science. 1998; 281:2016–2018. [PubMed: 9748158]

97. Bruchez M, Moronne M, Gin P, Weiss S, Alivisatos AP. Semiconductor nanocrystals as fluorescent biological labels. Science. 1998; 281:2013–2016. [PubMed: 9748157]

98. Cai WB, Chen K, Li ZB, Gambhir SS, Chen XY. Dual-function probe for PET and near-infrared fluorescence imaging of tumor vasculature. Journal of Nuclear Medicine. 2007; 48:1862–1870. [PubMed: 17942800]

99. Schipper ML, Cheng Z, Lee SW, Bentolila LA, Iyer G, Rao JH, Chen XY, Wul AM, Weiss S, Gambhirl SS. MicroPET-based biodistribution of quantum dots in living mice. Journal of Nuclear Medicine. 2007; 48:1511–1518. [PubMed: 17704240]

100. Yang HS, Santra S, Walter GA, Holloway PH. Gd-III-functionalized fluorescent quantum dots as multimodal imaging probes. Advanced Materials. 2006; 18:2890–2894.

101. Wang S, Jarrett BR, Kauzlarich SM, Louie AY. Core/shell quantum dots with high relaxivity and photoluminescence for multimodality imaging. Journal of the American Chemical Society. 2007; 129:3848–3856. [PubMed: 17358058]

102. Prinzen L, Miserus RJJHM, Dirksen A, Hackeng TM, Deckers N, Bitsch NJ, Megens RTA, Douma K, Heemskerk JW, Kooi ME, Frederik PM, Slaaf DW, van Zandvoort MAMJ, Reutelingsperger CPM. Optical and magnetic resonance imaging of cell death and platelet activation using annexin A5-functionalized quantum dots. Nano Letters. 2007; 7:93–100. [PubMed: 17212446]

103. Boersma HH, Kietselaer BLJH, Stolk LML, Bennaghmouch A, Hofstra L, Narula J, Heidendal GAK, Reutelingsperger CPM. Past, present, and future of annexin A5: From protein discovery to clinical applications. Journal of Nuclear Medicine. 2005; 46:2035–2050. [PubMed: 16330568]

104. Zhang CF, Jugold M, Woenne EC, Lammers T, Morgenstern B, Mueller MM, Zentgraf H, Bock M, Eisenhut M, Semmler W, Kiessling F. Specific targeting of tumor angiogenesis by RGD-conjugated ultrasmall superparamagnetic iron oxide particles using a clinical 1.5-T magnetic resonance scanner. Cancer Research. 2007; 67:1555–1562. [PubMed: 17308094]

105. Mulder WJM, Strijkers GJ, Nicolay K, Griffioen AW. Quantum dots for multimodal molecular imaging of angiogenesis. Angiogenesis. 2010; 13:131–134. [PubMed: 20552267]

106. Mulder WJM, Castermans K, van Beijnum JR, Egbrink MGAO, Chin PTK, Fayad ZA, Lowik CWGM, Kaijzel EL, Que I, Storm G, Strijkers GJ, Griffioen AW, Nicolay K. Molecular imaging

of tumor angiogenesis using alpha v beta 3-integrin targeted multimodal quantum dots. Angiogenesis. 2009; 12:17–24. [PubMed: 19067197]

107. Mulder WJM, Strijkers GJ, Van Tilborg GAF, Cormode DP, Fayad ZA, Nicolay K. Nanoparticulate Assemblies of Amphiphiles and Diagnostically Active Materials for Multimodality Imaging. Accounts of Chemical Research. 2009; 42:904–914. [PubMed: 19435319]

108. Mulder WJM, Koole R, Brandwijk RJ, Storm G, Chin PTK, Strijkers GJ, Donega CD, Nicolay K, Griffioen AW. Quantum dots with a paramagnetic coating as a bimodal molecular imaging probe. Nano Letters. 2006; 6:1–6. [PubMed: 16402777]

109. Santra S, Yang HS, Holloway PH, Stanley JT, Mericle RA. Synthesis of water-dispersible fluorescent, radio-opaque, and paramagnetic CdS: Mn/ZnS quantum dots: A multifunctional probe for bioimaging. Journal of the American Chemical Society. 2005; 127:1656–1657. [PubMed: 15700997]

110. Mulder WJM, Strijkers GJ, Habets JW, Bleeker EJW, van der Schaft DWJ, Storm G, Koning GA, Griffioen AW, Nicolay K. MR molecular imaging and fluorescence microscopy for identification of activated tumor endothelium using a bimodal lipidic nanoparticle. FASEB Journal. 2005; 19:2008–2010. [PubMed: 16204353]

111. Vuu K, Xie JW, McDonald MA, Bernardo M, Hunter F, Zhang YT, Li K, Bednarski M, Guccione S. Gadolinium-rhodamine nanoparticles for cell labeling and tracking via magnetic resonance and optical imaging. Bioconjugate Chemistry. 2005; 16:995–999. [PubMed: 16029042]

112. Kamaly N, Kalber T, Ahmad A, Oliver MH, So PW, Herlihy AH, Bell JD, Jorgensen MR, Miller AD. Bimodal paramagnetic and fluorescent liposomes for cellular and tumor magnetic resonance imaging. Bioconjugate Chemistry. 2008; 19:118–129. [PubMed: 17985841]

113. Vucic E, Sanders HMHF, Arena F, Terreno E, Aimo S, Nicolay K, Leupold E, Dathe M, Sommerdijk NAJM, Fayad ZA, Mulder WJM. Well-Defined, Multifunctional Nanostructures of a Paramagnetic Lipid and a Lipopeptide for Macrophage Imaging. Journal of the American Chemical Society. 2009; 131:406–407. [PubMed: 19105654]

114. Laurent S, Elst LV, Wautier M, Galaup C, Muller RN, Picard C. In vitro characterization of the Gd complex of [2,6-pyridinediylbis(methylene nitrilo)] tetraacetic acid (PMN-tetraacetic acid) and of its Eu analogue, suitable bimodal contrast agents for MRI and optical imaging. Bioorganic & Medicinal Chemistry Letters. 2007; 17:6230–6233. [PubMed: 17889530]

115. Li ZQ, Zhang Y. Facile synthesis of lanthanide nanoparticles with paramagnetic, down- and up-conversion properties. Nanoscale. 2010; 2:1240–1243. [PubMed: 20648356]

116. Li ZQ, Zhang Y, Shuter B, Idris NM. Hybrid Lanthanide Nanoparticles with Paramagnetic Shell Coated on Upconversion Fluorescent Nanocrystals. Langmuir. 2009; 25:12015–12018. [PubMed: 19764797]

117. Esfand R, Tomalia DA. Poly(amidoamine) (PAMAM) dendrimers: from biomimicry to drug delivery and biomedical applications. Drug Discovery Today. 2001; 6:427–436. [PubMed: 11301287]

118. Kobayashi H, Brechbiel MW. Dendrimer-based nanosized MRI contrast agents. Current Pharmaceutical Biotechnology. 2004; 5:539–549. [PubMed: 15579043]

119. Sarin H, Kanevsky AS, Wu HT, Brimacombe KR, Fung SH, Sousa AA, Auh S, Wilson CM, Sharma K, Aronova MA, Leapman RD, Griffiths GL, Hall MD. Effective transvascular delivery of nanoparticles across the blood-brain tumor barrier into malignant glioma cells. Journal of Translational Medicine. 2008; 6:1–15. [PubMed: 18171482]

120. Boswell CA, Eck PK, Regino CAS, Bernardo M, Wong KJ, Milenic DE, Choyke PL, Brechbiel MW. Synthesis, characterization, and biological evaluation of integrin alpha(v)beta(3)-targeted PAMAM dendrimers. Molecular Pharmaceutics. 2008; 5:527–539. [PubMed: 18537262]

121. Talanov VS, Regino CAS, Kobayashi H, Bernardo M, Choyke PL, Brechbiel MW. Dendrimer-based nanoprobe for dual modality magnetic resonance and fluorescence imaging. Nano Letters. 2006; 6:1459–1463. [PubMed: 16834429]

122. Pittet MJ, Swirski FK, Reynolds F, Josephson L, Weissleder R. Labeling of immune cells for in vivo imaging using magnetofluorescent nanoparticles. Nature Protocols. 2006; 1:73–79.

123. Manciulea A, Baker A, Lead JR. A fluorescence quenching study of the interaction of Suwannee River fulvic acid with iron oxide nanoparticles. Chemosphere. 2009; 76:1023–1027. [PubMed: 19477482]

124. Wang AZ, Bagalkot V, Vasilliou CC, Gu F, Alexis F, Zhang L, Shaikh M, Yuet K, Cima MJ, Langer R, Kantoff PW, Bander NH, Jon SY, Farokhzad OC. Superparamagnetic iron oxide nanoparticle-aptamer bioconjugates for combined prostate cancer imaging and therapy. Chemmedchem. 2008; 3:1311–1315. [PubMed: 18613203]

125. Kircher MF, Weissleder R, Josephson L. A dual fluorochrome probe for imaging proteases. Bioconjugate Chemistry. 2004; 15:242–248. [PubMed: 15025519]

126. Sosnovik DE, Garanger E, Aikawa E, Nahrendorf M, Figueiredo JL, Dai GP, Reynolds F, Rosenzweig A, Weissleder R, Josephson L. Molecular MRI of Cardiomyocyte Apoptosis With Simultaneous Delayed Enhancement MRI Distinguishes Apoptotic and Necrotic Myocytes in vivo: Potential for Midmyocardial Salvage in Acute Ischemia. Circulation. 2009; 120:S367–S367.

127. Sosnovik DE, Schellenberger EA, Nahrendorf M, Novikov MS, Matsui T, Dai G, Reynolds F, Grazette L, Rosenzweig A, Weissleder R, Josephson L. Magnetic resonance imaging of cardiomyocyte apoptosis with a novel magneto-optical nanoparticle. Magnetic Resonance in Medicine. 2005; 54:718–724. [PubMed: 16086367]

128. Wang DS, He JB, Rosenzweig N, Rosenzweig Z. Superparamagnetic Fe2O3 Beads-CdSe/ZnS quantum dots core-shell nanocomposite particles for cell separation. Nano Letters. 2004; 4:409–413.

129. Chen DY, Jiang MJ, Li NJ, Gu HW, Xu QF, Ge JF, Xia XW, Lu JM. Modification of magnetic silica/iron oxide nanocomposites with fluorescent polymethacrylic acid for cancer targeting and drug delivery. Journal of Materials Chemistry. 2010; 20:6422–6429.

130. Ma ZY, Dosev D, Nichkova M, Dumas RK, Gee SJ, Hammock BD, Liu K, Kennedy IM. Synthesis and characterization of multifunctional silica core-shell nanocomposites with magnetic and fluorescent functionalities. Journal of Magnetism and Magnetic Materials. 2009; 321:1368–1371. [PubMed: 20336173]

131. Lee JE, Lee N, Kim H, Kim J, Choi SH, Kim JH, Kim T, Song IC, Park SP, Moon WK, Hyeon T. Uniform Mesoporous Dye-Doped Silica Nanoparticles Decorated with Multiple Magnetite Nanocrystals for Simultaneous Enhanced Magnetic Resonance Imaging, Fluorescence Imaging, and Drug Delivery. Journal of the American Chemical Society. 2010; 132:552–557. [PubMed: 20017538]

132. Mandal SK, Lequeux N, Rotenberg B, Tramier M, Fattaccioli J, Bibette J, Dubertret B. Encapsulation of magnetic and fluorescent nanoparticles in emulsion droplets. Langmuir. 2005; 21:4175–4179. [PubMed: 15835991]

133. Park JH, von Maltzahn G, Ruoslahti E, Bhatia SN, Sailor MJ. Micellar hybrid nanoparticles for simultaneous magnetofluorescent imaging and drug delivery. Angewandte Chemie-International Edition. 2008; 47:7284–7288.

134. Roullier V, Grasset F, Boulmedais F, Artzner F, Cador O, Marchi-Artzner V. Small Bioactivated Magnetic Quantum Dot Micelles. Chemistry of Materials. 2008; 20:6657–6665.

135. Agrawal P, Strijkers GJ, Nicolay K. Chitosan-based systems for molecular imaging. Advanced Drug Delivery Reviews. 2010; 62:42–58. [PubMed: 19861142]

136. Ge YQ, Zhang Y, He SY, Nie F, Teng GJ, Gu N. Fluorescence Modified Chitosan-Coated Magnetic Nanoparticles for High-Efficient Cellular Imaging. Nanoscale Research Letters. 2009; 4:287–295. [PubMed: 20596545]

137. Li LL, Chen D, Zhang YQ, Deng ZT, Ren XL, Meng XW, Tang FQ, Ren J, Zhang L. Magnetic and fluorescent multifunctional chitosan nanoparticles as a smart drug delivery system. Nanotechnology. 2007; 18:1–6.

138. Tan WB, Zhang Y. Multi-functional chitosan nanoparticles encapsulating quantum dots and Gd-DTPA as imaging probes for bio-applications. Journal of Nanoscience and Nanotechnology. 2007; 7:2389–2393. [PubMed: 17663257]

139. Zhang YX, Das GK, Xu R, Tan TTY. Tb-doped iron oxide: bifunctional fluorescent and magnetic nanocrystals. Journal of Materials Chemistry. 2009; 19:3696–3703.

140. Selvan ST, Patra PK, Ang CY, Ying JY. Synthesis of silica-coated semiconductor and magnetic quantum dots and their use in the imaging of live cells. Angewandte Chemie-International Edition. 2007; 46:2448–2452.

141. Kim YB, Bae KH, Yoo SS, Park TG, Park H. Positive contrast visualization for cellular magnetic resonance imaging using susceptibility-weighted echo-time encoding. Magnetic Resonance Imaging. 2009; 27:601–610. [PubMed: 19106021]

142. Zhuo JC, Gullapalli RP. AAPM/RSNA physics tutorial for residents - MR artifacts, safety, and quality control. Radiographics. 2006; 26:275–U333. [PubMed: 16418258]

143. Yoon MA, Kim SH, Park HS, Lee DH, Lee JY, Han JK, Choi BI. Value of Dual Contrast Liver MRI at 3.0 T in Differentiating Well-Differentiated Hepatocellular Carcinomas From Dysplastic Nodules Preliminary Results of Multivariate Analysis. Investigative Radiology. 2009; 44:641–649. [PubMed: 19724237]

144. Sung CK, Hong KA, Lin S, Lee Y, Cha J, Lee JK, Hong CP, Han BS, Jung SI, Kim SH, Yoon KS. Dual-Modal Nanoprobes for Imaging of Mesenchymal Stem Cell Transplant by MRI and Fluorescence Imaging. Korean Journal of Radiology. 2009; 10:613–622. [PubMed: 19885318]

145. Small WC, Nelson RC, Bernardino ME. Dual Contrast Enhancement of Both T1-Weighted and T2-Weighted Sequences Using Ultrasmall Superparamagnetic Iron-Oxide. Magnetic Resonance Imaging. 1993; 11:645–654. [PubMed: 8345779]

146. Corot C, Robert P, Idee JM, Port M. Recent advances in iron oxide nanocrystal technology for medical imaging. Advanced Drug Delivery Reviews. 2006; 58:1471–1504. [PubMed: 17116343]

147. De Cuyper M, Soenen SJH, Coenegrachts K, Ter Beek L. Surface functionalization of magnetoliposomes in view of improving iron oxide-based magnetic resonance imaging contrast agents: Anchoring of gadolinium ions to a lipophilic chelate. Analytical Biochemistry. 2007; 367:266–273. [PubMed: 17568553]

148. Choi JS, Lee JH, Shin TH, Song HT, Kim EY, Cheon J. Self-Confirming "AND" Logic Nanoparticles for Fault-Free MRI. Journal of the American Chemical Society. 2010; 132:11015–11017. [PubMed: 20698661]

149. Bae KH, Kim YB, Lee Y, Hwang J, Park H, Park TG. Bioinspired Synthesis and Characterization of Gadolinium-Labeled Magnetite Nanoparticles for Dual Contrast T-1- and T-2-Weighted Magnetic Resonance Imaging. Bioconjugate Chemistry. 2010; 21:505–512.
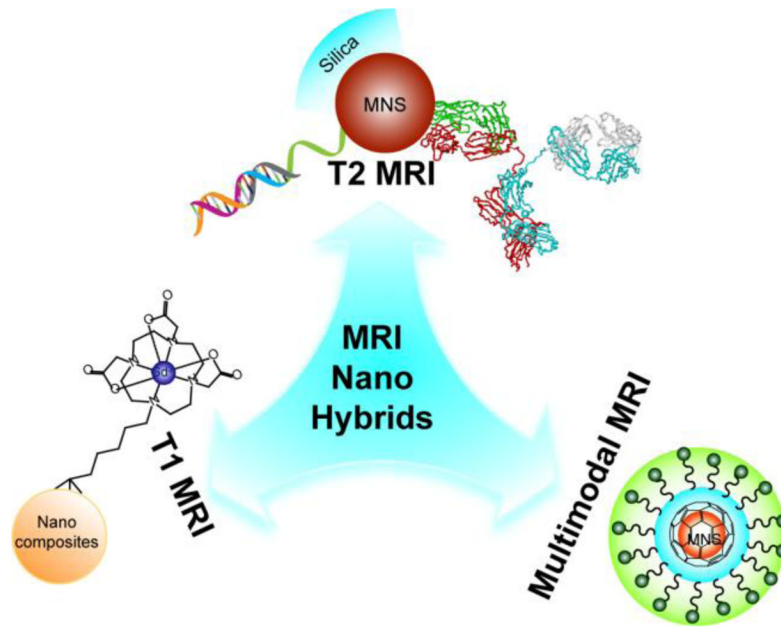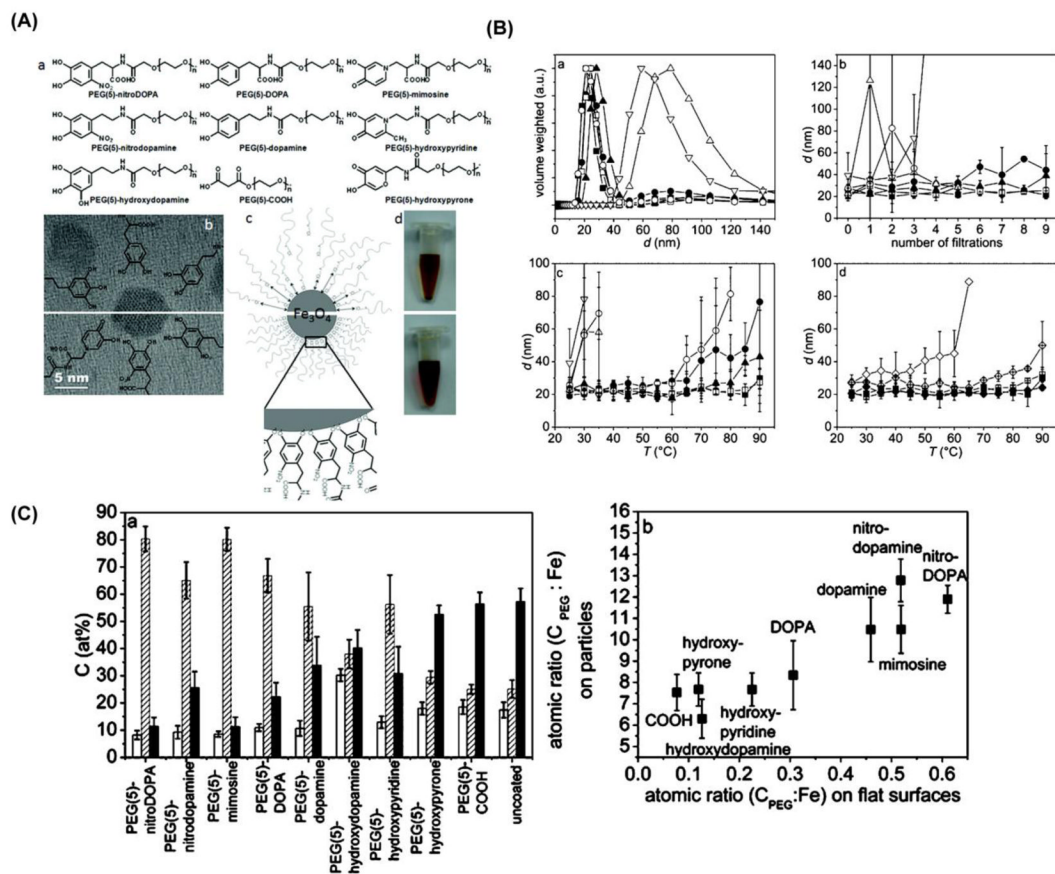
Figure 1.
Nanohybrid based various MR imaging agents.
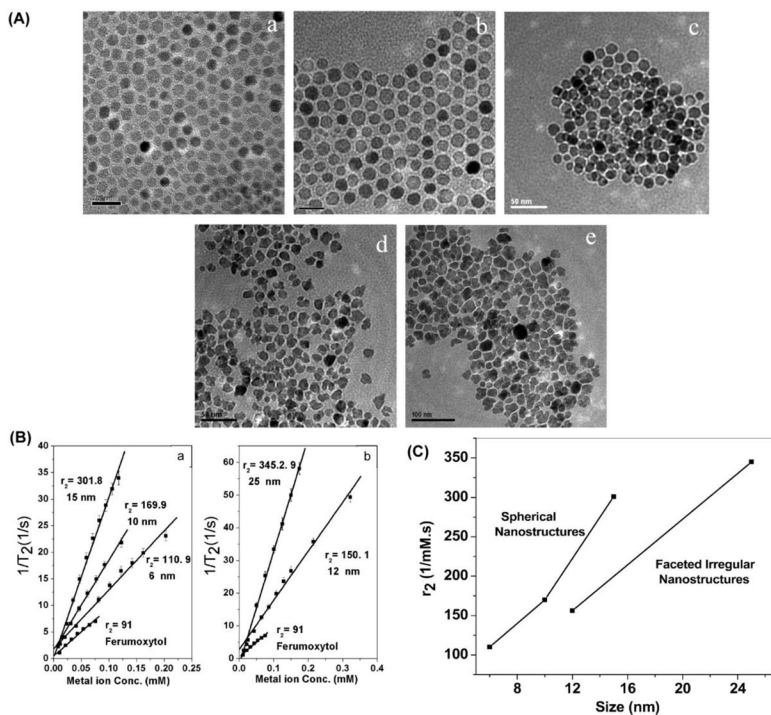
Figure 2.
MR properties of MNS is dependent on shape and size. (A) Synthesis results of various $CoFe_2O_4$ based on size, and shape regularity. It can be seen that pictures in A.a,b,c are spherical in nature, while A.d,e are faceted irregular (FI). (B). Relaxivity properties of MNS. (C). FI MNS demonstrate lower R_2 values for a given size (as measured by longest diameter across). [30]
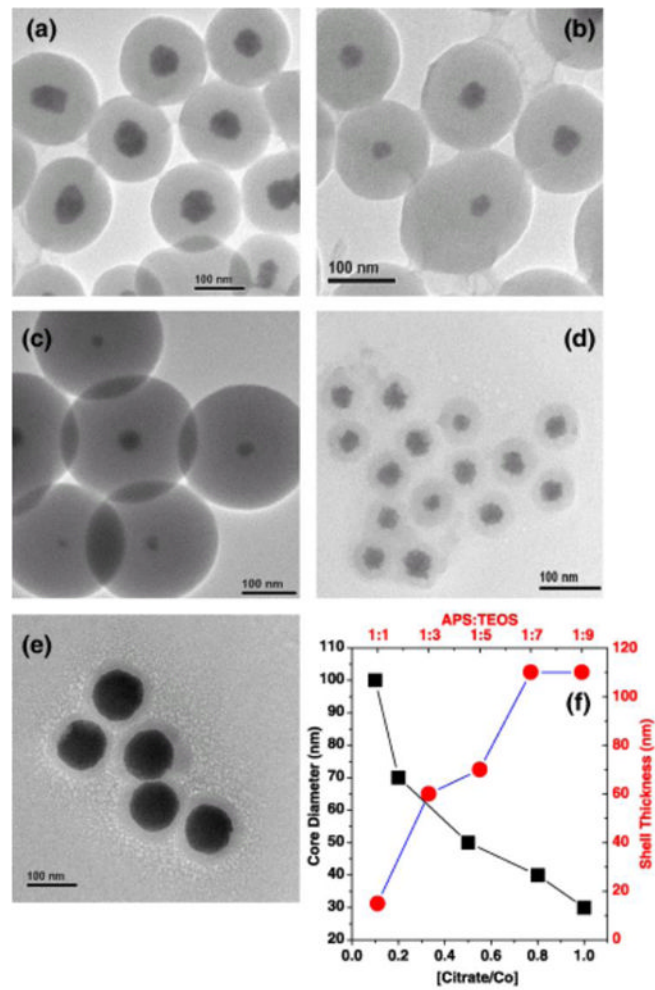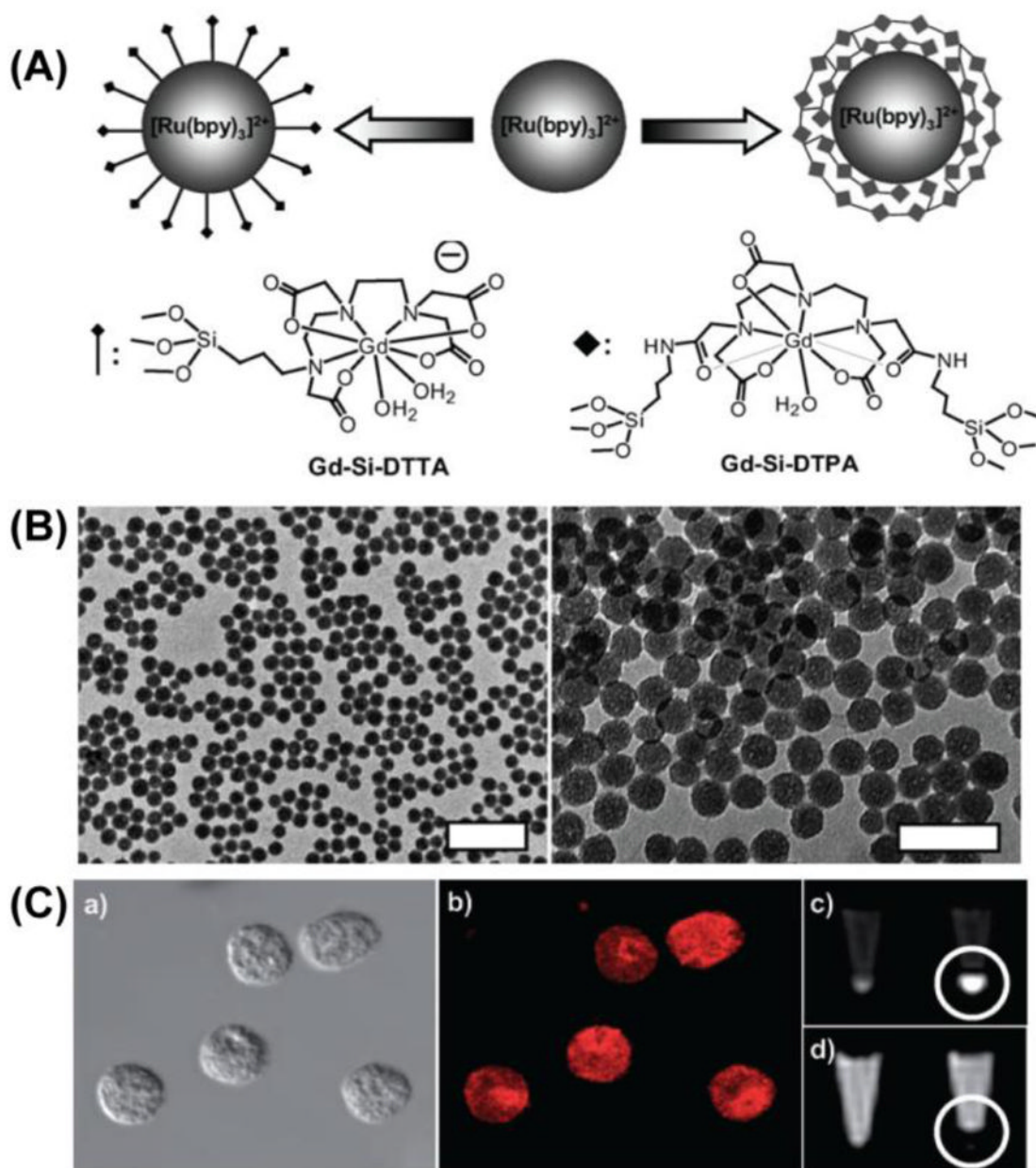
Figure 3.
Co MNS can be controllably encapsulated in silica shell by manipulation of TEOS precursor ratio. Additionally, core diameter can be manipulated through capping ligand addition [38].

Figure 4.
(A) Stabilization of iron oxide MNS using various catechol derivative as anchor group. (B) DLS measurements of individually stabilized iron oxide nanoparticles based on their aqueous stability (a), effect on filtration (b) and the stability as a function of temperature (c). (C) The dispersants ligands absorbed on 2D and nanoparticle surface as measured by XPS.

Figure 5.
(**A**) Synthetic procedure of low and high pay load hybrid silica nanoparticle with [Ru(bpy)$_3$]Cl$_2$ and Gd^{3+}. (**B**) TEM of above synthesized nanoparticles, showing the larger surface area of six times higher loaded gadolinium ion. The scale bar represents 200 nm (left) and 100 nm respectively. (**C**) Microscopic images of hybrid silica nanoparticles labeled monocyte cells: a) optical; b) laser scanning confocal fluorescence. c), d) MR images of unlabeled (left) and 1-labeled monocyte cells: c) T$_1$-weighted and d) T$_2$-weighted [92].
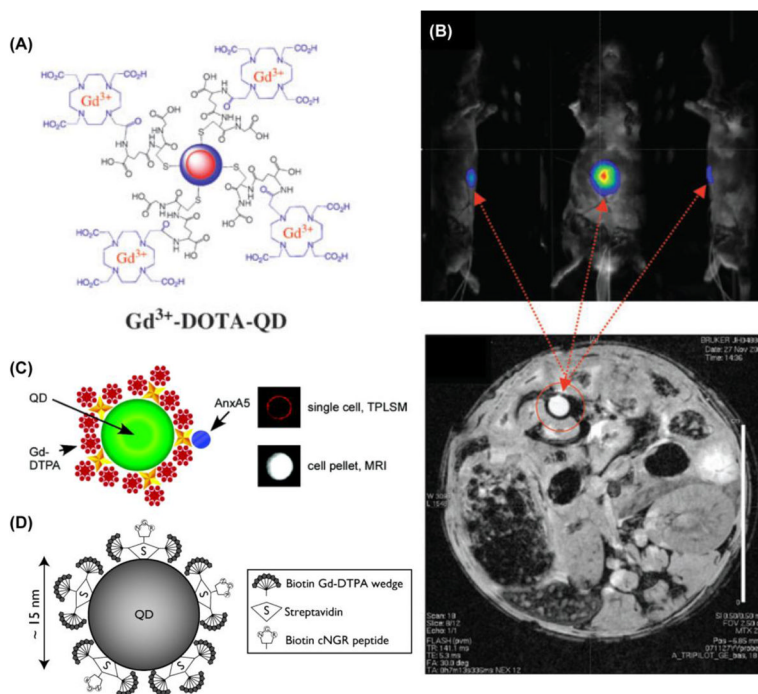
Figure 6.
(**A**) Gd^{3+}-DOTA functionalized CdSeTe/CdS QDs with glutathione (GSH) coating. (**B**) A NIR-fluorescence image [42] and T_1 weighted MR image (bottom) of a mouse. A phantom containing 10 µM of Gd^{3+}-DOTA-QDs was visualized by both fluorescence imaging and MRI. (**C**) QD with the biotinylated Gd-wedge, containing eight Gd-DTPA complexes with AnaxA5 (AnxA5-QD-Gd-wedge). This nanohybrid can be visualized by both fluorescence and MR imaging. (**D**) Schematic representation of a cNGR-labeled paramagnetic quantum dot. Commercially available this QD carries ~10 streptavidin moieties to which 6 cNGR groups and hence 24 gadolinium constructs were bound. Based on that estimation the maximum number of Gd^{3+} was 192 [102–104].
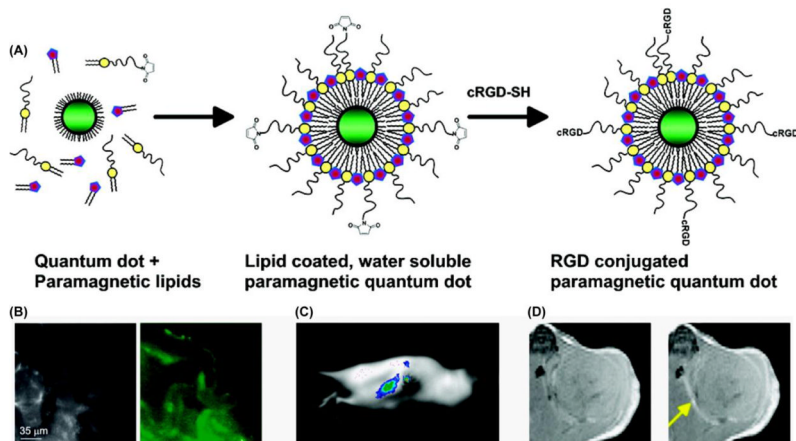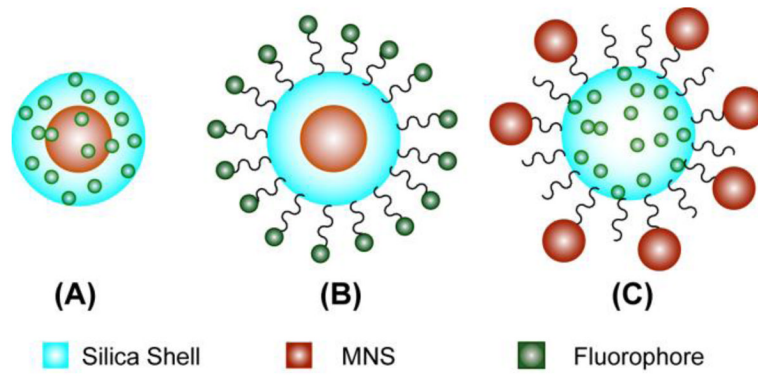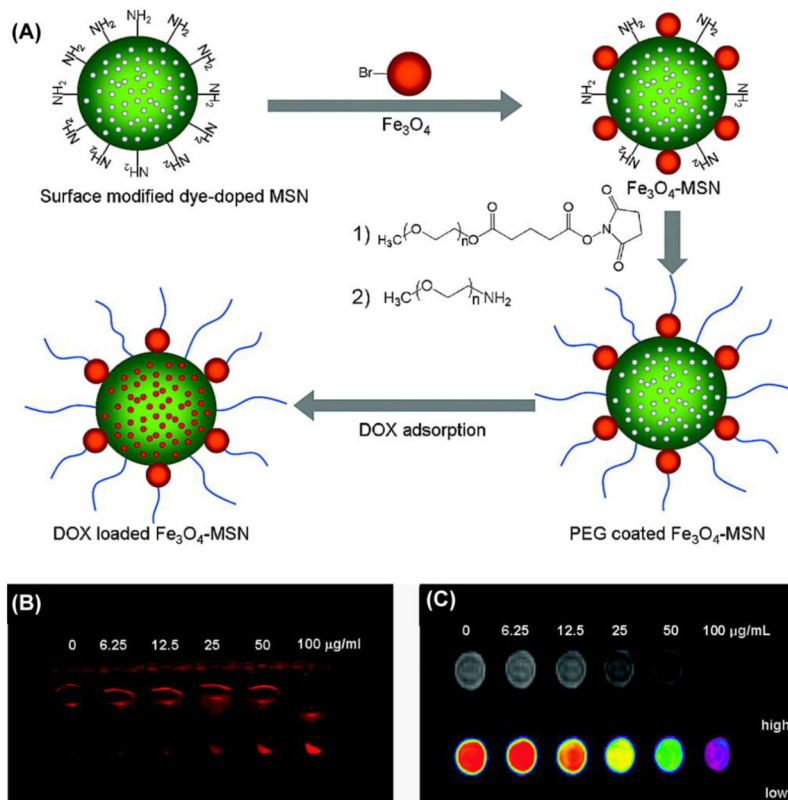
Figure 7.
(**A**) Schematic depiction of the preparation of liposome with a paramagnetic micellular coating and targeting peptide. (**B**) The brightfield (left) and fluorescence image of tumor-bearing mice after intravenous injection of paramagnetic QDs. (**C**) Fluorescence image reveled the target specific accumulation of contrast agents. (**D**) T_1-weighted MR images before and 45 min after the injection of paramagnetic QD–micelles[106].
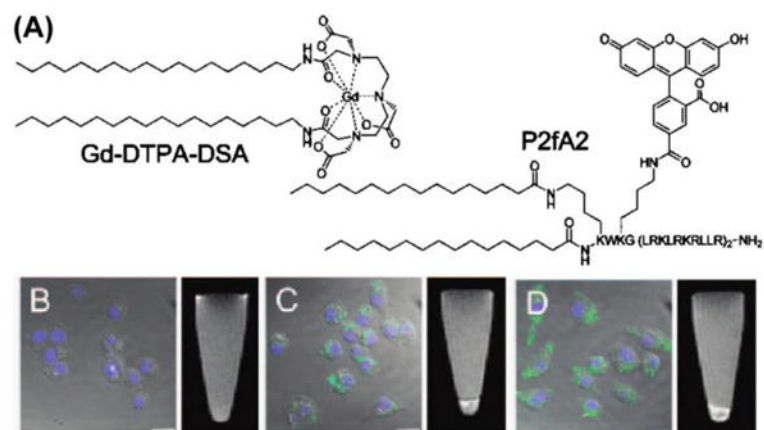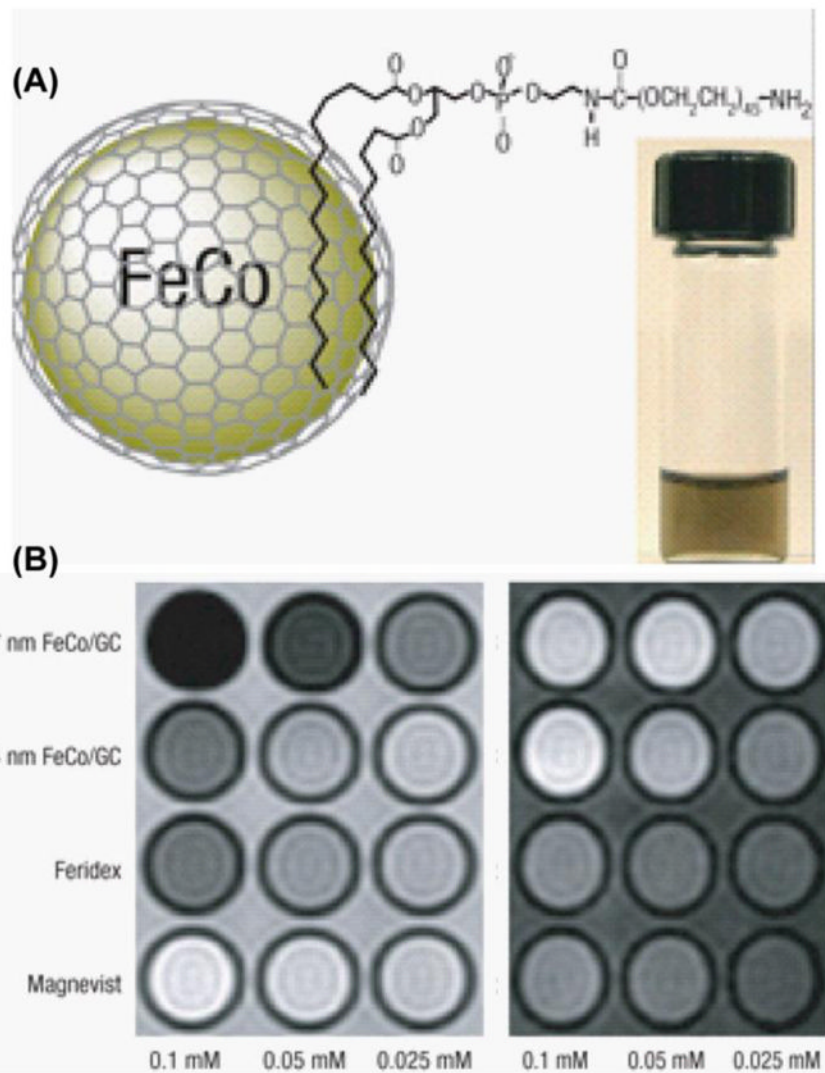
Figure 8.
(**A**) Structure of Gd^{3+} chelating lipid Gd-DTPA-DSA and fluorescein labeled apolipoprotein E derived lipopeptide, P2fA2. (**B–D**) Confocal and MRI of untreated (**B**), incubated with 33% (**C**) and (**D**) 50% **P2fA2** nanohybrid macrophage cell pellets. Scale bar: 20 μm [113].
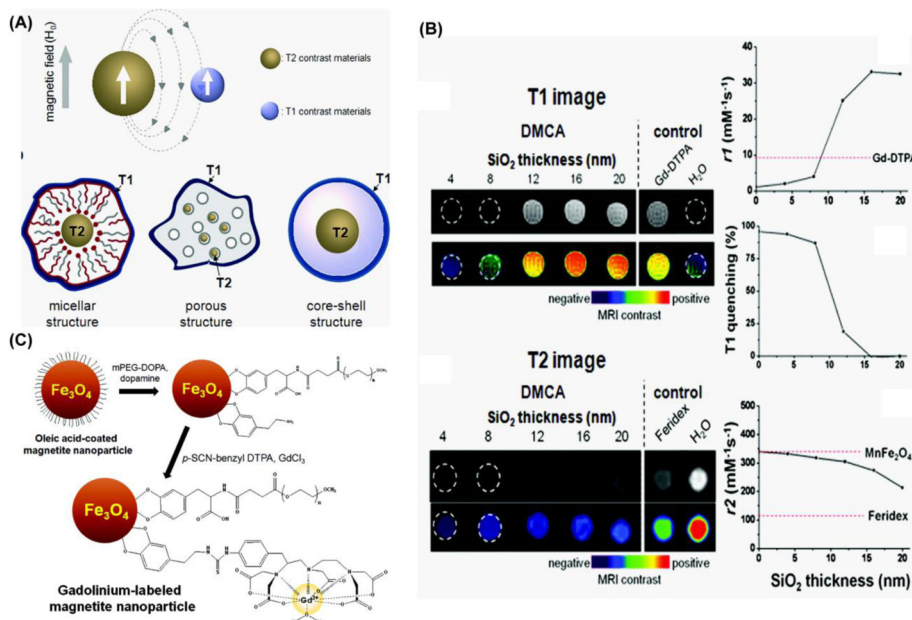
Figure 9.
Schematic presentation of various silica based optical-MNS nanohybrids. (**A**) Fluorophore doped MNS-Silica core-shell nanohybrids, (**B**) Fluorophore conjugated MNS-Silica core-shell nanohybrids and (**C**) MNS conjugated fluorophore doped silica nanohybrids.

Figure 10.
(**A**) Schematic depiction of the synthetic procedure for Fe_3O_4-MSN (mesoporous silica nanoparticle), stabilization by PEG and loading of DOX (doxorubicin). (**B,C**) In vitro multimodal imaging of drug loaded MNS-silica nanohybrids, (**B**) fluorescence image (**C**) MRI image at different concentrations [131].

Figure 11.
(**A**) Schematic diagram of phospholipid stabilized FeCo/graphite shell nanocrystal and a PBS suspension after heating to 80 °C for 1 h (inset). (**B**) T_2 (left) and T_1 weighted MR images of various contrast agents at three metal concentrations [50].

Figure 12.
(A) Magnetic coupling between T_1 and T_2 contrast materials and the possible structures of various T_1/T_2 bimodal MRI contrast agent. (B) T_1 and T_2 MR imaging of MnFe$_2$O$_4$-Gd MNS with a variable thickness of SiO$_2$ shell. With increasing SiO$_2$ layer R_1 increases and R_2 decreases. (C) Synthesis of gadolinium-labeled MNS as a dual contrast agent for T_1 and T_2 weighted magnetic resonance imaging [148].

Table 1

Summary of some select T_2 and T_1 contrast agents and their material properties.

Name	Core material	Surface coating	Core Diam.[45]	Outer Diam.[45]	R_1 (mM^{-1}s$^{-1)}$	R_2 (mM^{-1}s^{-1})
Ferumosil (AMI-121)	Fe$_3$O$_4$[46]	Silica/Siloxane[46]	10	12[46]	n/a	n/a
				300[40]		
Ferumoxide (AMI-125)	Fe$_3$O$_4$[46]	Dextran[46]	5[46]	12[46]	10.1 (@1.42T)[22]	120 (@1.42T)[22]
				120–180[47]	5 (@3T)[22]	130 (@3T)[22]
					1.8 (@7.1T)[22]	132 (@7.1T)[22]
Ferumoxtran-10 (AMI-227)	Fe$_3$O$_4$[46]	Dextran[46]	6[46]	16[46]	9.9 (@1.42T)[22]	65 (@1.42T)[22]
					5 (@3T)[22]	66 (@3T)[22]
				15–30[48]	1.4 (@7.1T)[22]	71 (@7.1T)[22]
PEG-magnetite(polyol)[49]	Fe$_3$O$_4$	TREG	8	16.5	14.14 (@1.5T)	82.68 (@1.5T)
Spherical Cobalt Ferrite[30]	CoFe$_2$O$_4$	11-AUA*	15	~15	n/a	301.8 (@1.5T)
FI Cobalt Ferrite$^¥$[30]	CoFe$_2$O$_4$	11-AUA*	12	~15	n/a	150.1 (@1.5T)
Silica coated magnetite[32]	γ-Fe$_2$O$_3$	N/A	10±2	10±2	n/a	228 (@11.7T)
	γ-Fe$_2$O$_3$	Silica	10±2	14±2	n/a	100 (@11.7T)
	γ-Fe$_2$O$_3$	Silica	10±2	27±5	n/a	64 (@11.7T)
	γ-Fe$_2$O$_3$	Silica	10±2	50±7	n/a	38 (@11.7T)
Magnetite[31]	Fe$_3$O$_4$	DMSA	12	15	n/a	218 (@1.5T)
Manganese ferrite[31]	MnFe$_3$O$_4$	DMSA	12	15	n/a	358 (@1.5T)
Cobalt Ferrite[31]	CoFe$_3$O$_4$	DMSA	12	15	n/a	172 (@1.5T)
Iron-Cobalt[50]	FeCo	Graphite/phospholipid-PEG	7	30	70	644 (@1.5T)

* 11-amino undecanoic acid,

$^¥$ FI: Faceted Irregular, n/a – not available